Nonlinear Hydrodynamic Loads on Offshore Wind Turbine Support Structures

Wave Kinematics Modelling for Monopile Design for Extreme Wave Events

in partial fulfillment of the requirements for the degree of

Master of Science

in Offshore and Dredging Engineering
at Delft University of Technology

Author: Leonard Vos
Student number: 5655811
Project duration: January 1, 2024 – October 31, 2024

Comitee:	Dr. ir. P. R. Wellens,	Delft University of Technology - Chairman
	Dr. ir. I. Akkerman	Delft University of Technology
	Dr. ir. D. P. Rijnsdorp,	Siemens Gamesa
	Ir. M. van der Meulen,	Siemens Gamesa

TU Delft SIEMENS Gamesa
RENEWABLE ENERGY

Preface

This master thesis is submitted as partial fulfilment of the requirements for the degree of Master of Science in Offshore and Dredging Engineering at the Delft University of Technology. The work has been conducted in collaboration with Siemens Gamesa Renewable Energy. Daily supervision was provided by Dirk Rijnsdorp and Michiel van der Meulen from SGRE and Peter Wellens was the supervisor from TU Delft.

I would like to express my sincere gratitude to Dirk and Michiel for their valuable supervision, insightful feedback, and ideas throughout this project. The almost weekly catch-up meetings with Dirk were particularly helpful and greatly contributed to the progress of my work. A special thanks to Peter for providing inspiration and high-level ideas during the project, as well as for chairing the committee. Our meetings not only brought up key suggestions and directions for the project but also allowed for enjoyable conversations about our mutual interest in cycling. I am grateful to all the fellow students I met during my thesis journey. Sharing the ups and downs of the master thesis experience, supporting each other through the rough times, and enjoying various activities, related to our studies or not, made the process more meaningful and rewarding. A big thank you to the colleagues at SGRE for providing much-needed breaks and distractions from work with a "potje". Special gratitude to Colinda for always bringing positivity and handling all administrative matters. Last, but certainly not least, thanks to my friends and family for their mental support, engaging conversations, and thought-provoking questions that helped me clarify my ideas.

Abstract

Accurate modelling of ultimate or maximum hydrodynamic loads is crucial for the design of offshore wind turbines and ensure the survivability for its design life time. High fidelity direct Fluid-Structure Interaction models can provide accurate results but are too computationally expensive to deploy for the many environmental loading conditions that need to be evaluated during the design phase. Indirect numerical methods that separately obtain the wave kinematics and subsequently use those to calculate the hydrodynamic loads are widely used in the industry. Often extended linear wave theory is deployed to obtain the kinematics. However, for storm wave conditions and breaking wave events, this theory breaks down and requires engineering solutions such as separate slamming models to provide conservative force estimations. Fully nonlinear wave kinematics might directly represent steep and breaking waves, omitting the requirement of slamming models.

This study evaluates the performance of the non-hydrostatic wave model SWASH in simulating fully nonlinear wave kinematics that are subsequently used to obtain the hydrodynamic loads with the Morison equation. The project focuses on the extreme events of a typical 50 year return period storm in the North Sea. Deterministic comparison of the time series of the hydrodynamic loads of the nonlinear model with available experimental data and a linear model, that served as a benchmark representing the industry method, showed mixed results. Several large overshoots were observed in the nonlinear results for non extreme events, which were not present in the experimental data. Load estimates for extreme events were of mixed accuracy, both over and under estimations of the hydrodynamic load magnitudes were observed. The study concludes that while SWASH offers valuable insights into nonlinear wave dynamics, further refinement is needed to improve its reliability in load predictions. Future research should initially focus on refining the implementation of SWASH, tackling the large overshoots by including a wave breaking turbulence model.

Contents

List of Figures

List of Tables

Nomenclature

Physical constants and quantities		**Value**	**SI unit**
ρ	(Sea) water density	1025	kg/m^3
g	Acceleration due to gravity	9.81	m/s^2

Wave parameters		
η	Free-surface elevation	m
H	Wave height	m
$\overline{H}$	Mean wave height	m
H_s	Significant wave height	m
H_{m0}	Spectral significant wave height	m
H_b	Breaking wave height	m
a	Wave amplitude	m
T	Wave period	s
T_z	Mean or zero-crossing period	s
T_b	Breaking wave period	s
f	Frequency	Hz
f_{peak}	Peak frequency	Hz
ω	Wave angular frequency	rad/s
φ	Phase angle	rad
λ	Wavelength	m
k	Wave number	1/m
c	Wave celerity	m/s
d	Water depth from MSL	m
h	Length of the water column	m

Kinematic parameters		
η_b	Free-surface elevation at the boundary	m
$\boldsymbol{u}$	Fluid particle velocity vector	m/s
u_x	Horizontal fluid particle velocity (x-direction)	m/s
u_y	Horizontal fluid particle velocity (y-direction)	m/s
u_z	Vertical fluid particle velocity (z-direction)	m/s
a_x	Horizontal fluid particle acceleration (x-direction)	m/s^2
a_z	Vertical fluid particle acceleration (z-direction)	m/s^2
P	Total fluid pressure	Pa
p	Dynamic fluid pressure	Pa
q	Non-hydrostatic fluid pressure	Pa
ν	Dynamic viscosity water	kg/ms
ϕ	Velocity potential	m^2/s
ϕ_w	Linear wave velocity potential	m^2/s
$E/E1/E2(z)$	Depth decay function	
z'	Stretched vertical coordinate	

Hydrodynamic load parameters

f	Distributed inline wave-induced force	N/m
f_{ad}	Distributed axial divergence correction force	N/m
C_M	Inertia coefficient	
C_a	Added mass coefficient	
C_D	Drag coefficient	
D	Pile diameter	m
F_{shear}	Shear force	N
$M_{ovt.}$	Overturning moment	Nm
KC	Keulegan-Carpenter number	
F_s	Total slamming force	N
f_s	Distributed slamming force	N/m
τ_b	Slamming event duration	s
F_b	Peak slamming force	N
κ	Curling factor	
C_s	Slamming coefficient	
$g(t)$	Temporal distribution slamming event	
$G_y(z)$	Spatial distribution slamming event	
T_s	Duration of the slamming event	s
F_{m0}	Significant force peak	N
M_{m0}	Significant moment peak	Nm

Mathematical operators

$\nabla\cdot$	Divergence
∇	Gradient
$\nabla\times$	Curl
$H\{...\}$	Imaginary part of Hilbert transform
$< ... >$	Time average of signal

Statistical and spectral parameters

μ	Expected value	
$p(x)$	Probability density	
$S(f)$	Variance density	m^2/Hz
m_0	Zeroth spectral moment	m^2
Δf	Frequency bandwidth	Hz
α	Phillips constant	
γ	Peak enhancement factor	
σ	Peak width parameter	

1

Introduction

1.1. Background

The need to combat climate change is pressing many countries and companies to seek sustainable energy solutions to reach their commitments to become carbon net zero. Relying on a single renewable energy source will not be sufficient; a mix of various renewable energy solutions is required to achieve climate goals [8]–[10]. Wind power plays an important role in this renewable mix. A recent report from Wind Europe states that the annual installation capacity of wind farms over the period of 2024 to 2030 is estimated at 29 gigawatts (GW), of which a significant part will be offshore [11], see Figure 1.1.

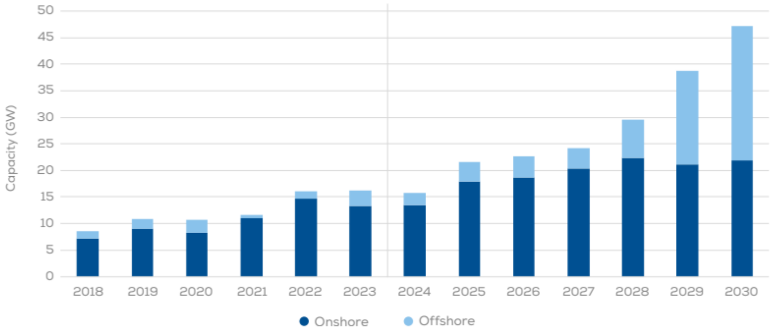

Figure 1.1: Annual onshore and offshore wind power installations in the EU [11].

Compared to onshore, offshore wind offers more consistent and higher wind speeds, which are advantageous for maximizing energy generation. Additionally, placing turbines several kilometres out at sea addresses common "Not In My Backyard" (NIMBY) concerns such as visual impact, noise, and potential effects on property values. Offshore wind farms avoid these issues, enabling larger installations with less local resistance.

A significant trend in the offshore wind industry is the increasing size of turbines. As blade lengths grow, the swept area increases, boosting the turbine's energy production potential. This allows for greater electricity generation per turbine and reduces the cost per unit of energy by spreading fixed costs over a larger output. Furthermore, fewer but larger turbines can reduce environmental impact while optimizing energy production per area.

The increase in size is made possible by advances in materials, aerodynamics, and control systems. Turbine size is typically denoted in terms of power rating, the maximum amount of power the turbine can generate. In the 1990s, turbines were under 1 MW with rotor diameters around 35 meters. By the early 2000s, sizes grew to 2-3 MW with diameters up to 80 meters. The 2010s saw turbines reach 6-8 MW and rotor diameters around 150-170 meters. In recent years, turbines have reached capacities of 12-15 MW with rotor diameters exceeding 200 meters, such as the GE Haliade-X and SG 14-222 DD [12]. The growth in turbine size shows no signs of stopping, with the next generation of wind turbines already announced with power ratings reaching 22 MW [13]. Figure 1.2 shows the trend of offshore turbine size growth that are in development phase for the period 1980-2030.

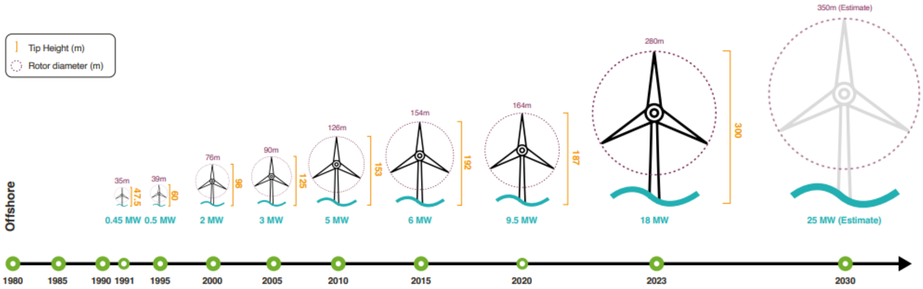

Figure 1.2: Offshore wind turbine growth trend 1980-2030 [1].

Several types of support structures exist for offshore turbines, both floating and bottom-fixed. An overview of the most popular is presented in Figure 1.3. The choice of structure type usually depends on the water depth and soil conditions. The most common bottom-fixed support structure type is the monopile, which is used for almost all turbines installed in the North Sea. Monopiles offer simplicity, a large steel pile driven into the seabed, and adaptability, which allows for design optimizations at specific turbine locations. As power ratings and rotor diameters increase for larger turbines, the tower and monopile diameters must also increase. The current generation of 10-15 MW wind turbines requires monopiles with diameters between 8 and 10 meters [14][15]. Next-generation wind turbines will require even larger monopile diameters.

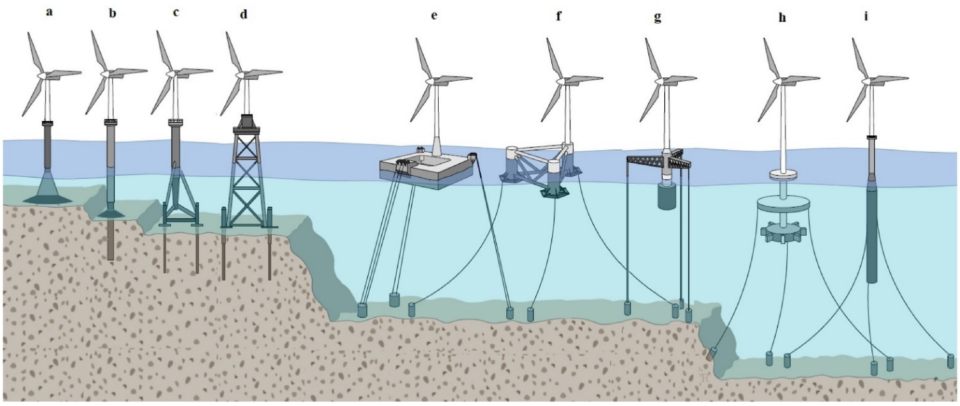

Figure 1.3: Different offshore wind turbine support structure types for bottom fixed: a) gravity based, b) monopile, c) tripod, d) jacket. For floating wind turbines: e) buoyancy (with damping pool), f) buoyancy (semi-submerged), g) tension leg platform (TLP), h) and i) spar (ballast) [2].

The marine environment poses significant challenges for offshore wind turbines due to constant exposure to high winds, strong waves, and corrosive saltwater. These harsh conditions not only accelerate material degradation but also subject the structures to extreme dynamic loads, which must be considered during the design phase.

Focusing on the waves, hydrodynamic forces are a major design challenge for the support structures. As turbine sizes and monopile diameters increase, the impact of wave-induced loads grows significantly, scaling with the square of the monopile diameter. One of the key challenges is the impact of hydrodynamic forces on the support structures. As turbine sizes and monopile diameters increase, the effect of wave-induced loads becomes more significant, scaling with the square of the monopile diameter. Accurate prediction of these forces is crucial for ensuring the stability and longevity of the wind turbine's support system. Detailed modelling is required to capture the dynamic effects of storm waves. Therefore, reliable load models are critical to ensure prevention of structural failure over the turbine's 20-25 year design life.

The current best practice that is adopted by the industry, is designing based on 50-year return period loads [16]–[18]. These loads are determined from environmental conditions that have a probability of occurrence of 2% or once every 50 years. When these storms occur in certain areas, the waves can reach such a height or steepness that they become unstable and break. Breaking waves near offshore wind turbines can cause much higher loads than non-breaking waves with similar height and period, often by a factor of up to 2.8 [6].

Physical experiments, even on model-scale, are too time consuming and costly to perform during the design process. As a cost-effective alternative, numerical modelling is widely used, with methods divided into direct and indirect approaches. High fidelity direct fluid-structure interaction (FSI) methods, such as Computational Fluid Dynamics (CFD), simulate the dynamic interaction between waves and the monopile in real-time, capturing both the impact of the waves on the structure and the structure's response on the surrounding fluid. Indirect methods initially determine the wave motion characteristics, which can subsequently be converted into hydrodynamic forces using a suitable force model.

While high fidelity models provide the most realistic results, they also require significant computational resources. Therefore, in industry, lower fidelity, more time efficient indirect methods are preferred. The wave motion characteristics (wave kinematics) can be obtained with linear theory, such as Airy wave theory [19], that may be extended by including higher order wave theory to model a single extreme design wave. Linear wave theory is based on the assumption that the wave amplitudes are small and is therefore not suited for representing high and steep storm waves. A practical solution is to embed a single nonlinear extreme wave in the linear time series. Some examples are the embedded stream function wave [20] and NewWave theory [21].

When wave kinematics are known, the corresponding hydrodynamic loads on submerged structures can be determined. For slender structures such as monopiles, the Morison equation [22] is a widely used and effective approach. This method models the hydrodynamic force as the superposition of two components: drag, related to fluid velocity, and inertia, associated with fluid acceleration. By incorporating fluid and structural properties, along with appropriate drag and inertia coefficients, the loads can be accurately calculated. The equation is semi-empirical and is widely adopted in the industry due to its proven reliability in predicting hydrodynamic loads.

Modelling extreme or breaking wave events is difficult because of their highly nonlinear, unpredictable nature, involving rapid, short-duration forces, complex fluid dynamics, and turbulent interactions between air and water. Direct methods like CFD incorporate these aspects and can give more accurate estimations of the hydrodynamic loads. But again, they are also more computationally expensive and unfeasible due to time constraints during the design phase. Instead of capturing the actual breaking wave behaviour, a workaround solution for indirect methods is to simply add an additional term to the force equation. Several wave impact or slamming models have been proposed [6], [7], [23] but these are based on many simplifications and assumptions. Furthermore, these methods are empirical in nature and require calibration for site specific cases. At present, there is no general slamming model that can accurately predict breaking wave loads under all possible conditions.

To summarize, multiple sources of uncertainty are present in modelling storm-condition hydrodynamic loading on offshore wind support structures. The first source arises from the assumptions and simplifications required in numerical models to deliver results within design phase time constraints. These uncertainties are further amplified when modelling breaking wave events, where their unpredictable and highly variable nature introduces additional complexity. While high fidelity numerical models can estimate hydrodynamic loads with greater accuracy, their computational cost is often prohibitive, especially during the design phase. Given the increasing size of turbines and the growing significance of hydrodynamic loads in design, these challenges highlight the need for more accurate and efficient modelling methods for storm wave conditions.

1.2. Research objective

This project aims to address these challenges by contributing to the development of a model that offers more accurate and reliable predictions of hydrodynamic loads on monopile support structures under storm wave conditions and during extreme events. While direct FSI methods offer detailed insights, their high computational cost limits their practicality for routine use, reserving them primarily for specific research or validation studies.

For design purposes, predicting hydrodynamic loads through pre-calculated wave kinematics is generally more efficient than using direct FSI methods. Pre-calculating wave kinematics enables reuse across multiple design iterations, avoiding the need to rerun costly simulations each time the structural design is adjusted. Therefore, this research will focus on indirect methods. More specifically, this research project focuses on improving the accuracy of wave kinematics. Several sources of uncertainty were identified, both within existing kinematic models and the unpredictable nature of breaking waves. To address these uncertainties, instead of relying on extensions of linear theory using higher-order design waves, fully nonlinear wave kinematics will be utilized. Nonlinear kinematics offer a more comprehensive solution by capturing wave dynamics over the entire simulation duration, providing a more accurate representation of complex wave phenomena.

This approach is particularly well-suited for modelling storm waves, where nonlinear effects, including wave steepening and breaking, become more significant. For offshore wind turbine structures, accurately capturing these nonlinear interactions is essential for predicting extreme hydrodynamic loads and ensuring structural stability, especially during severe storm events, such as those seen in 50-year return period conditions.

Several higher-order wave models are available, each with its own advantages and limitations:

- Boussinesq-type models (e.g. FUNWAVE [24]) are effective in shallow water but are limited in intermediate depths due to their depth-averaged approach and reliance on higher-order derivatives to approximate vertical accelerations. Therefore, to capture wave breaking, simplifications must be introduced.

- Nonlinear potential flow models (e.g. OceanWave3D [25]) methods are efficient in simulating nonlinear wave dynamics, including wave steepening while maintaining relatively low computational cost. However, potential flow cannot inherently simulate breaking waves and would cause numerical instabilities. A non-physical filter must therefore be introduced that includes numerical damping.

- Non-hydrostatic models are particularly valuable because they directly incorporate vertical accelerations into their governing equations, making them more accurate for simulating critical processes like wave steepening and the lead up process of wave breaking, especially under storm conditions. Unlike models that rely on breaking filters, non-hydrostatic models can resolve these processes more physically.

In this project, SWASH, an open-source, multi-purpose non-hydrostatic model [26], will be employed to simulate nonlinear wave kinematics.

The Morison equation will be deployed to determine the hydrodynamic loads. The total force is represented as the superposition of drag and inertia forces, which can be readily derived from fluid velocities and accelerations. Hydrodynamic load time series are essential in the design phase, particularly for determining the ultimate limit state (ULS). By analysing these time series, engineers can identify peak forces and moments under varying wave conditions, which are critical for ensuring structural stability and safety. A research objective can now be formulated:

> *The objective of this research is to evaluate the performance of the non-hydrostatic model SWASH in simulating fully nonlinear wave kinematics. These kinematics will be used in combination with the Morison equation to estimate hydrodynamic loads under typical 50-year return period storm conditions in the North Sea, particularly for extreme events.*

To achieve the research objective, the nonlinear wave model will be both validated and compared to existing methods. Available experimental data will be used for validation, providing a robust foundation to test the model's accuracy. In addition, the nonlinear model will be compared against a linear, industry-standard model to assess performance improvements. This linear model serves as a benchmark, offering insight into the advantages of incorporating nonlinearities.

Particular attention will be given to extreme events within the experimental hydrodynamic time series, as peak forces and moments are often associated with breaking waves. A key question is whether the nonlinear kinematics, as modelled by SWASH, can capture the behaviour of breaking waves and translate these dynamics into accurate hydrodynamic loads through the Morison equation. The ability of the model to represent transient behaviours during such extreme events will also be closely examined.

In addressing this research objective, the study seeks to fill the existing knowledge gap regarding the accuracy of nonlinear kinematics derived from SWASH, specifically in capturing breaking wave events, and whether these nonlinear kinematics can be effectively translated into accurate impact loads using the Morison equation. Additionally, this research will assess the overall performance of the nonlinear model under storm conditions, offering insight into its applicability for offshore wind turbine structural design.

1.3. Thesis structure

The research project begins with a literature review. The necessary background knowledge is outlined in chapter 2. This chapter starts by discussing methods to mathematically describe waves in section 2.1. Various approaches for obtaining wave kinematics are introduced in section 2.2, where linear wave theory is derived and nonlinear perturbation methods are briefly mentioned. The wave breaking process and its modeling techniques are described in section 2.3. Section 2.4 covers the theoretical background of the nonlinear numerical wave model SWASH. Finally, the hydrodynamic force model is discussed in section 2.5, including the basic model, extensions, and methods for modeling breaking waves or slamming forces.

Chapter 3 details the methodologies and data sources used for the analysis, starting with an overview of the available experimental data in section 3.1. The wave model implementations, linear and SWASH, are provided in section 3.2 and application of the Morison equation is discussed in section 3.3.

Validation results of the nonlinear model are presented in chapter 4. The main findings and results of the performance evaluation are discussed in chapter 5. Interpretation of the results, along with discussions of limitations and recommendations, are provided in chapter 6. Finally, the key findings are summarized and concluded in chapter 7.

2

Theoretical background

This chapter presents the essential background knowledge, methods, and theories required to eventually calculate hydrodynamic loads on offshore support structures. The focus of this project is on eventually calculating hydrodynamic loads on the support structure of offshore wind turbines. As discussed in the previous section, indirect methods that first obtain wave kinematics and then determining the wave-induced loads, are employed.

Before discussing wave or hydrodynamic models in detail, it is important to first introduce how ocean waves are characterized and understood. When standing on the beach observing the ocean, the surface may appear messy and chaotic, but there are underlying patterns and principles that govern wave behaviour. This chapter begins by outlining the methodology used to systematically describe ocean waves in section 2.1.

Once a mathematical representation of waves is established, the next step is to explore how their behaviour and motion can be numerically modelled. Many of these methods are derived from the fundamental fluid equations known as the Navier-Stokes equations, first developed by Claude-Louis Navier [27] and later refined by George Gabriel Stokes [28]. Section 2.2 will discuss analytical methods and begins with the general formulation, and through a series of assumptions, potential flow theory will be derived. Then, the linear wave theory concepts, based on potential flow theory, will be presented. More complex nonlinear theories will also be briefly introduced to address phenomena that go beyond the scope of linear approximations, including wave breaking and interactions in extreme conditions.

Since storm wave conditions, where wave breaking can occur, are the primary focus of this project, section 2.3 describes the mechanics of wave breaking and how they can be modelled numerically. Following this, the selected nonlinear numerical model will be introduced in section 2.4, where a brief overview of the governing equations is presented. This section also outlines the relevant options for inflow and outflow conditions, as well as the approach used to model wave breaking.

With a thorough understanding of wave kinematics and the numerical modelling of wave behaviour, the next step is to focus on the calculation of hydrodynamic loads on monopiles. One of the most widely used approaches for determining hydrodynamic forces on slender offshore structures is the Morison equation [22], due to its effectiveness in modelling wave-induced loads on monopiles. Section 2.5 will provide a detailed discussion of the Morison equation, outlining its derivation, key assumptions, and how it can be applied to calculate hydrodynamic loads based on the previously introduced wave kinematics. A commonly used method for incorporating breaking wave loads is to include a slamming model, where the slamming force is superimposed on the hydrodynamic loads obtained from linear theory. A brief overview of these methods will be provided.

2.1. Ocean waves description

In order to model ocean waves numerically, they first need to be mathematically defined. This section will begin by introducing the definitions and characteristics of regular waves. Then, the descriptions of irregular waves will be provided, followed by a discussion on the statistical properties of irregular waves and sea states.

2.1.1. Regular waves

The free surface elevation as a function of time $\eta(t)$ at a fixed location of a regular linear wave can be described as a sinusoidal wave, with an amplitude a, frequency f and a phase angle φ:

$$\eta(t) = a\cos(2\pi f t + \varphi) \tag{2.1}$$

The wave height H is the total height from trough to crest and double the amplitude. Figure 2.1 provides both a temporal (left) and spatial (right) snapshot of a regular wave.

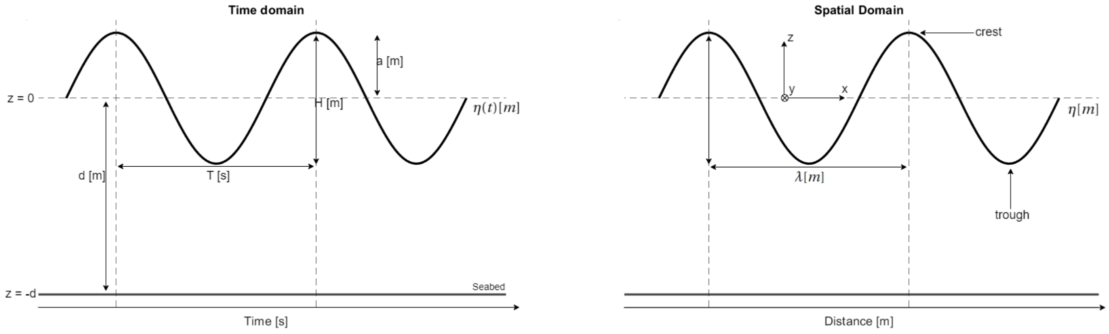

Figure 2.1: Wave characteristics and definitions. On the left hand, a wave is measured at a fixed location over time (temporal domain), and on the right-hand side, a snapshot of a wave in time is presented (spatial domain).

The positive vertical direction is upwards and the mean sea level (MSL) is at $z = 0$. As can be seen on the left side of Figure 2.1, the time it takes for one full wave to pass is defined as the wave period $T = 1/f$. When a snapshot in time is taken, on the right side of Figure 2.1, the wavelength λ can be defined as the distance between two crests. The propagation velocity of the wave, also known as wave celerity or phase velocity, is defined as $c = \lambda/T$. The water depth d is defined downwards from the MSL to the seafloor at $z = -d$.

2.1.2. Irregular waves

Irregular waves or sea states can be described as a summation of many sinusoidal waves, with individual amplitudes, frequencies, phases and directions. The superposition principle is visualised in Figure 2.2. Irregular waves can be described with an irregular wave model that is based on this superposition principle, the random phase/amplitude model:

$$\eta(t) = \sum_{i=1}^{N} a_i \cos(2\pi f_i t + \varphi_i) \tag{2.2}$$

Where $\eta(t)$ is the surface elevation, and a_i, f_i, and φ_i are the amplitudes, frequencies, and phases, respectively. Describing one observation of ocean waves is often not feasible nor preferable. Ocean waves are random in nature, and it makes more sense to describe the sea surface as a stochastic process. Hence, the amplitudes and phase angles are treated as random variables. The amplitudes follow a Rayleigh distribution and the phase angles a uniform distribution between 0 and 2π and the probability density functions (pdf) read as follows:

$$p(\alpha_i) = 1/2\pi \quad \text{for} \quad 0 < \alpha_i < 2\pi \tag{2.3}$$

$$p(a_i) = \frac{\pi}{2}\frac{a_i}{\mu_i^2}\exp\left(-\frac{\pi a_i^2}{4\mu_i^2}\right) \quad \text{for} \quad a_i > 0 \tag{2.4}$$

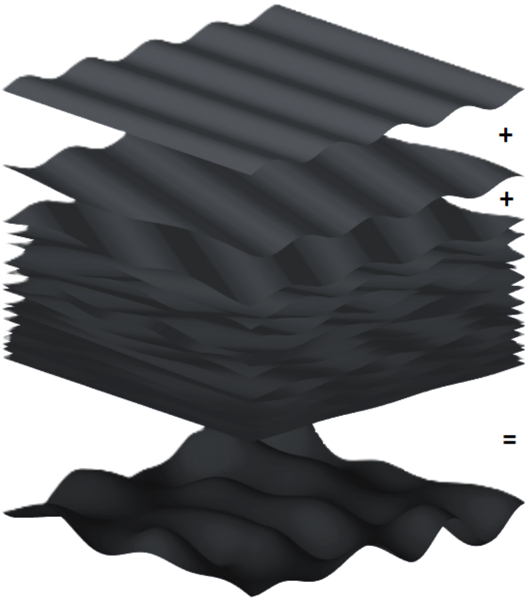

Figure 2.2: Superposition principle for irregular waves.

Here, $\mu_i = E\{\underline{a}_i\}$ is the expected value of the amplitude. The underlying assumptions for the random phase/amplitude model are that the free-surface time series is (approximately) stationary and that the harmonic components are independent and thus linear.

Often, a variance spectrum is used to describe the free-surface elevation. The variance $E\{\underline{a}_i^2\}$ is statistically relevant quantity and is directly proportional to the physical energy of the waves. The variance spectrum, is described in discrete frequency components, whereas a real wave spectrum at sea describes a continuum of frequencies. By distributing the variance of the frequency interval, the variance density spectrum is obtained. A typical variance density spectrum that is used for wave generation is the JONWSWAP spectrum. It is the result of an extensive data collection study from the North Sea during the Joint North Sea Wave Observation Project (JONSWAP) [29]. The JONSWAP spectrum describes an undeveloped sea state. Out at sea, the waves in the frequency range considered here are generated by the wind. When the wind has been blowing steadily over a very long distance and for a very long period, the sea state is considered fully developed and the waves are in equilibrium with the wind. The Pierson-Moskowitz spectrum [30] describes such a fully developed sea state.

However, the research project concluded that sea states are very rarely fully developed. The proposed spectrum for an undeveloped sea state is an adaptation of the Pierson-Moskowitz spectrum with a peak enhancement factor to fit the data from the measurements. The JONSWAP spectrum expression is as follows:

$$S(f) = \alpha g^2 (2\pi)^{-4} f^{-5} \exp\left(-\frac{5}{4}\left(\frac{f_{peak}}{f}\right)^{-4}\right)\gamma^{\Omega(f)} \tag{2.5}$$

$$\Omega(f) = \exp\left(-\frac{1}{2}\left(\frac{f/f_{peak}-1}{\sigma}\right)^2\right) \tag{2.6}$$

Where α is the Phillips constant, sometimes called the energy scale parameter, g the gravitational acceleration, f_{peak} the frequency scale parameter or the peak frequency, γ is the peak-enhancement factor (typically 3.3) and σ is the peak-width parameter. These parameters have been determined empirically and depend on the met-ocean conditions. The combination of a (significant) wave height, peak period or frequency and a spectrum shape is often denoted as a sea state. A sea state refers therefore to the overall condition of the free-surface elevation.

2.1.3. Time-frequency domain transformation

Transformations from the frequency domain (e.g. JONSWAP spectrum) to time domain (free-surface elevation time series) and vice versa are essential for analysis. For example, a free-surface time series measurement can be transformed to the frequency domain through Fourier Series Analysis. The signal is decomposed into many harmonic components with an amplitude phase angle coupled to a discrete frequency. This allows for frequency analysis of the signal or using the Fourier Series as input for a numerical model. For the transformation from the frequency domain back to the time domain the random phase/amplitude model can be deployed. In this approach, the amplitude of each wave component is given by:

$$a_i = \sqrt{2S(f_i)\Delta f} \tag{2.7}$$

Where Δf is the frequency bandwidth. The phase angles φ_i are now randomly drawn from a uniform distribution between 0 and 2π. This process is shown in Figure 2.3.

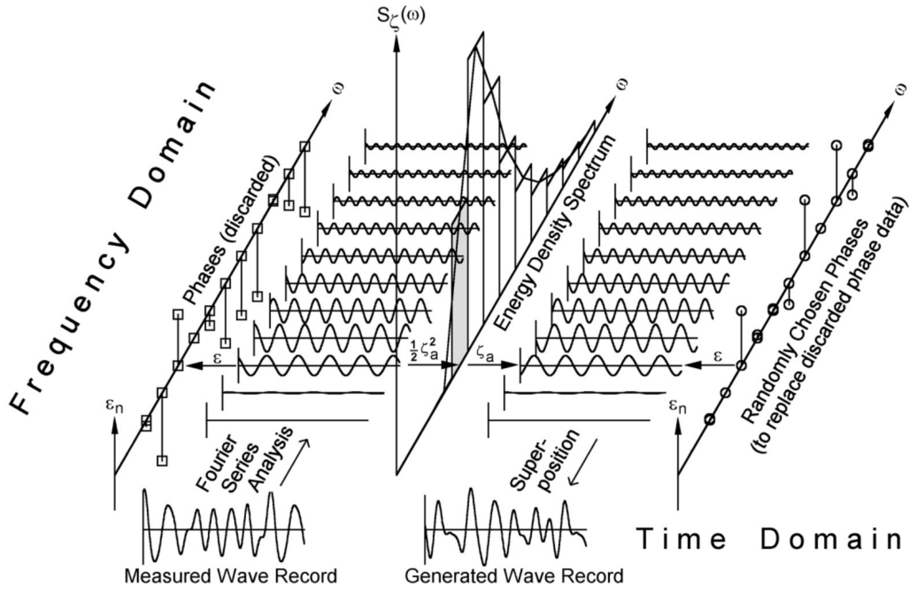

Figure 2.3: Transformation from a measured free-surface signal to a variance density spectrum and back to a generated free-surface signal. The time series are completely different but the statistical and spectral properties are the same [3].

When a measured signal must be reconstructed in, for example, a numerical model, the phase angles are required. Hence, when waves are generated from a variance density spectrum in a numerical model, the randomly drawn phase angles, often defined by a seed that is used for a random number generator, from the experiment are required. Otherwise, a Fourier Series analysis must be performed on a measured signal to obtain the phase angles.

2.1.4. Ocean wave statistics

The free-surface elevation does not have a constant wave height or period, it is therefore convenient to define the mean wave height and zero crossing period:

$$\overline{H} = \frac{1}{N}\sum_{i=1}^{N} H_i \tag{2.8}$$

$$\overline{T_z} = \frac{1}{N}\sum_{i=1}^{N} T_{z,i} \tag{2.9}$$

(2.10)

A wave period in a random free-surface signal is the time between two zero up- or down- crossings, when the wave elevation crosses the MSL. For a breaking wave the steep front is most relevant for the breaking process, which is included in the definition with downward crossings.

The wave height is then defined as the distance between the maximum and minimum elevation between the two zerod down-crossings. In ocean engineering it is common practice to use the significant wave height instead, defined as the mean of the one-third highest waves:

$$H_s = \frac{1}{N/3} \sum_{j=1}^{N/3} H_j \tag{2.11}$$

The significant wave height is useful because it can also be estimated from the variance density spectrum. The spectral significant wave height is defined as follows:

$$H_{m0} = 4\sqrt{m_0} \tag{2.12}$$

Where m_0 is the zeroth spectral moment. When the random free-surface elevation is treated as a stationary, Gaussian process, then all its statistical properties are determined from the variance density spectrum S(f) and are expressed in terms of spectral moments:

$$m_n = \int_0^\infty f^n S(f) df \tag{2.13}$$

The zeroth spectral moment, when $n = 0$, is the area under the curve and thus represents the total energy contained in the signal. Now that the ocean surface can be represented mathematically, the formulations for velocities and accelerations of the water can be derived.

2.2. Wave kinematics

Wave kinematics refer to the motion of water particles as waves propagate through a body of water. In general, waves do not cause net transport of mass but rather transfer energy through the water. The individual water particles move in a circular or elliptical motion and returning to their original position, shown in Figure 2.4. Water particle velocities and accelerations can be obtained either analytically or numerically. This section will focus on the analytical methods, of which an overview is shown in Figure 2.5. This graph is not directly applicable for irregular waves, as there is no single wavelength and wave height combination. Engineers often use the significant wave height and peak period to check which theory is applicable for the main component of the irregular wave spectra. First, the linear or Airy wave theory will be derived. Then, the nonlinear theories will be discussed.

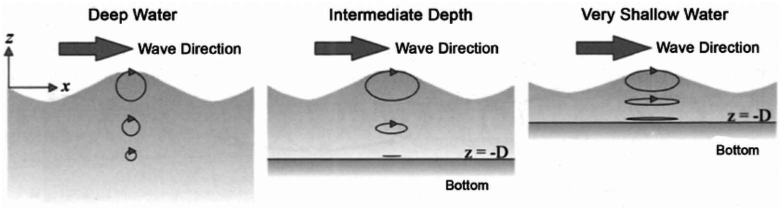

Figure 2.4: The orbital motions of water particles for deep, intermediate and shallow water [3].

2.2.1. Navier-Stokes equations

Several methods exist to obtain wave kinematics numerically and at the basis of almost all of them are the Navier-Stokes equations. The full Navier-Stokes equations describe viscous, rotational and incompressible fluid motion. The equations are a set of differential equations describing the conservation of mass, momentum and energy. In any fluid system, mass cannot be created or destroyed, only transferred within the system. It must therefore be conserved within the domain. The mathematical expression of mass conservation is the so-called continuity equation, here given for incompressible fluids:

$$\nabla \cdot \boldsymbol{u} = \frac{\partial u_x}{\partial x} + \frac{\partial u_y}{\partial y} + \frac{\partial u_z}{\partial z} = 0 \tag{2.14}$$

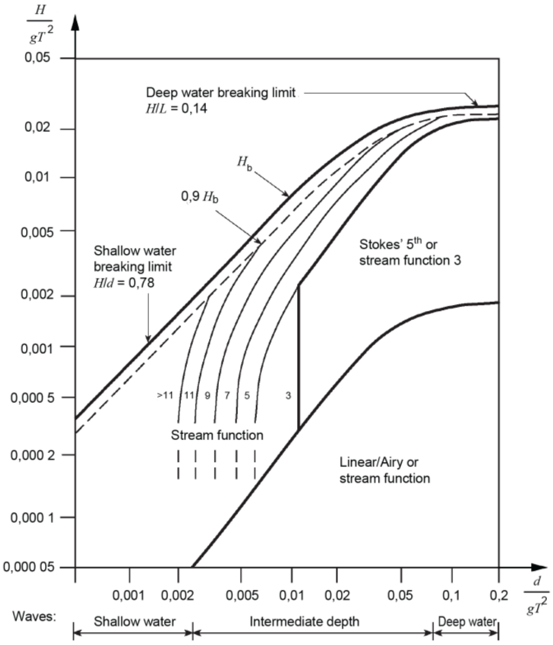

Figure 2.5: Dimensionless limits of validity for various theories for regular waves [4]

Where $\boldsymbol{u} = (u_x, u_y, u_z)$ is the fluid velocity vector with components u_x, u_y, u_z in the x, y, z directions respectively. The $\nabla\cdot$ is the divergence operator and measures the rate of expansion (or compression) of the velocity field. In the case of incompressible fluids, it indicates that there is no net change in fluid density in the control volume, the net inflow is equal to the net outflow rate.

The momentum equation is derived from Newton's second law describing the change of fluid momentum due to various forcing terms. The equation governs how the fluid velocity field evolves over time due to forces such as pressure gradients, viscous forces and external forces like gravity.

$$\frac{\partial \boldsymbol{u}}{\partial t} + (\boldsymbol{u}\cdot\nabla)\boldsymbol{u} - \nu\nabla^2\boldsymbol{u} = -\frac{1}{\rho}\nabla p + \boldsymbol{g} \tag{2.15}$$

ρ is the fluid density, $\frac{\partial}{\partial t}$ is the time derivative, ν is the dynamic viscosity, p is the pressure and $\boldsymbol{g}$ represents the external forces, gravity in this case. The expression of gravitational acceleration $\boldsymbol{g}$ in Cartesian coordinates is $\boldsymbol{g} = (0, 0, -g)$. The ∇ operator here is the gradient and measures the rate and direction of change in scalar fields.

The first two terms in the equation are the inertia terms, the local acceleration of the fluid and the convective acceleration. The last term on the left hand side is the viscous or diffusion term, accounting for the internal frictional forces acting on the fluid due to viscosity. This term drops out for in-viscous fluids. The first term on the right hand side is the (internal) pressure gradient, representing the force per unit volume exerted by pressure differences within the fluid. It drives the fluid motion from high pressure to low pressure regions. The last term is the external force. For the application of surface gravity waves the dominant external force is gravity. For very large or rotating systems the centrifugal or Coriolis force must be included as well.

The mass and momentum equations are sufficient to describe surface gravity wave motion because these waves are primarily driven by gravitational forces and fluid inertia, not thermal effects. The continuity equation ensures mass conservation, while the momentum equation captures the balance between gravitational forces and fluid acceleration. Incompressible water and negligible temperature variations allow for the energy conservation equation to be omitted for non-breaking waves. For breaking waves, the situation is more complex. The momentum equation needs to account for viscous forces, turbulence, and energy dissipation, and the energy conservation equation can no longer be ignored, see section 2.3.

2.2.2. Potential flow theory

The Navier-Stokes equations are highly nonlinear and often complex boundary conditions are present. Furthermore, turbulence in the flow is difficult to solve as it involves a large range of scales. These factors require high computational resources and it is therefore not practical for long duration simulations or during the design phase when relative quick results are required. However, simplified theories are often accurate enough to estimate the wave kinematics for obtaining the global hydrodynamic loads.

In Equation 2.14 and 2.15, already incompressibility is assumed. When the flow speed is much lower than the speed of sound in the fluid (1500 m/s for fresh water at room temperature), the fluid can be assumed incompressible which is the case for surface gravity waves. However, when the water at the surface is mixed with air, for example in the aftermath of or during wave breaking, the speed of sound through that mixture, can be significantly lower. Two phase flow modeling is not within the scope of this project but is important to keep in mind for (violent) wave breaking events. Furthermore, when the fluid is assumed in-viscid ($\nu = 0$), the viscous terms drops out resulting in the so-called Euler equations. The momentum conservation formula for inviscid flow is:

$$\frac{\partial \boldsymbol{u}}{\partial t} + (\boldsymbol{u} \cdot \nabla)\boldsymbol{u} = -\frac{1}{\rho}\nabla p + \boldsymbol{g} \tag{2.16}$$

Considering flows on the scale of surface gravity waves at sea, the inertia term dominates the viscous term which often allows for the viscous term to be neglected. Finally, the fluid is assumed irrotational. Irrotational flow means that the vorticity of the fluid is zero, which mathematically can be defined as the curl of the flow field being zero:

$$\nabla \times \boldsymbol{u} = 0 \tag{2.17}$$

$\nabla\times$ is thus the curl of the vector field and measures the tendency to rotate around a point, it represents the rotational component of the flow. Due to this assumption, the velocity field can be expressed as the gradient of a scalar potential ϕ:

$$\boldsymbol{u} = \nabla\phi \tag{2.18}$$

The velocity potential ϕ is a fundamental concept to describe irrotational flow. When the above is substituted in the continuity equation from 2.14, the Laplace equation is obtained:

$$\nabla \cdot \boldsymbol{u} = \nabla \cdot (\nabla\phi) = \nabla^2\phi = 0 \tag{2.19}$$

The Laplace equation describes the velocity potential in Potential flow theory. The Laplace equation is linear, which allows for superposition. Potential flow is a powerful tool for solving simplified flow problems. Solutions to the Laplace equation are defined by the boundary conditions.

2.2.3. Linear wave theory

Airy Wave Theory is based on potential flow with the above-mentioned assumptions (incompressible, inviscid, and irrotational). Furthermore, the wave amplitudes must be small relative to their wavelength. Here, the waves are assumed to be long crested, which simplifies the problem to two dimensions.

The Laplace equation is a second order partial differential equation and requires two boundary conditions. In this case, two kinematic conditions (describing the motion) are applied, one at the free-surface and one at the seabed. At the free-surface, no spray or mixing is allowed at the air-water interface, meaning that the water particles remain at the free-surface. The particle velocity normal to the free-surface must be equal to the velocity of the free-surface in that direction:

$$u_z = \frac{\partial\phi}{\partial z} = \frac{\partial\eta}{\partial t} \quad \text{at} \quad z = 0 \tag{2.20}$$

The second kinematic boundary condition ensures that the seabed is impermeable; water cannot flow through the seabed. The assumption here is that we have a flat or small angled seafloor. Hence, the vertical velocity at the seabed is zero:

$$u_z = 0 \quad \text{at} \quad z = -d \tag{2.21}$$

These two conditions link the velocity potential to the free-surface elevation and ensures that the surface moves in response to the underlying fluid flow, making sure that the velocity field determined by the Laplace equation is consistent with the actual motion of the water surface.

The momentum equation is first order and requires one boundary condition. Since the pressure is considered, a dynamic condition (describing forces) is applied:

$$p = 0 \quad \text{at} \quad z = 0 \tag{2.22}$$

The final boundary condition, describes the force relation or the dynamic condition at the free-surface. For the waves to be free, subject only to gravity and no external force, the atmospheric pressure at the free-surface must be constant, or simply zero. Note that the free-surface elevation boundary is defined at $z = 0$. In reality, the boundary is at $z = \eta$, the actual free-surface elevation. However, the equations then become nonlinear. The linearization step of setting the free-surface boundary conditions at $z = 0$ is allowed for small wave amplitudes as the distance between the mean sea level and the actual free-surface is small. When the kinematics are required above the mean water level up to the crest height, a stretching method can be applied, see subsection 2.2.4.

The dynamic boundary condition can be derived further by substituting $\boldsymbol{u}$ as the gradient of the velocity potential (2.18) in the momentum equation (2.16):

$$\frac{\partial \nabla \phi}{\partial t} + (\nabla \phi \cdot \nabla)\nabla \phi = -\frac{1}{\rho}\nabla p + \boldsymbol{g} \tag{2.23}$$

The second term on the left hand side is a nonlinear term that can be neglected when small wave amplitudes are assumed. When this equation is integrated over depth, and apply $p = 0$:

$$\frac{\partial \phi}{\partial t} + g\eta = 0 \quad \text{at} \quad z = 0 \tag{2.24}$$

An analytical solution of the Laplace Equation 2.19 is the harmonic propagating wave, see Equation 2.1, combined with the following wave velocity potential:

$$\phi_w(x,z,t) = a\omega \frac{\cosh(k(z+d))}{\sinh(kd)} \cos(kx - \omega t) \tag{2.25}$$

Where a is the wave amplitude, $\omega = 2\pi f$ is the angular frequency, $k = 2\pi/\lambda$ is the wave number, d is the total water depth. From the definition of potential theory, the particle velocities can now be obtained by taking the gradient of the velocity potential in the required direction. The horizontal and vertical velocity components are derived below:

$$u_x(x,z,t) = \frac{\partial \phi_w}{\partial x} = -a\omega k \cdot \frac{\cosh(k(d+z))}{\sinh(kd)} \cdot \sin(kx - \omega t) = a\omega k \cdot \frac{\cosh(k(d+z))}{\sinh(kd)} \cdot \sin(\omega t) \tag{2.26}$$

$$u_z(x,z,t) = \frac{\partial \phi_w}{\partial z} = a\omega k \cdot \frac{\sinh(k(d+z))}{\sinh(kd)} \cdot \cos(kx - \omega t) = a\omega k \cdot \frac{\sinh(k(d+z))}{\sinh(kd)} \cdot \cos(\omega t) \tag{2.27}$$

When x is assumed to be constant, the kx term can be omitted as the reference location can be chose at $x = 0$. Obtaining the acceleration terms is straight forward, the time derivative is taken from the velocity terms:

$$a_x(x,z,t) = \frac{\partial u}{\partial t} = a\omega^2 k \cdot \frac{\cosh(k(d+z))}{\sinh(kd)} \cdot \cos(\omega t) \tag{2.28}$$

$$a_z(x,z,t) = \frac{\partial w}{\partial t} = a\omega^2 k \cdot \frac{\sinh(k(d+z))}{\sinh(kd)} \cdot \sin(\omega t) \tag{2.29}$$

These are the most complete formulations of the wave kinematics. For relatively deep or shallow water, the hyperbolic depth decay functions can be simplified. In Figure 2.4 it was shown how the orbital path and velocity magnitudes depend on the water depth.

Another part of the solution of the Laplace equation entails the dispersion relationship. When the harmonic surface profile (Equation 2.1) and the velocity potential (Equation 2.18) into the free-wave condition (Equation 2.24), the following can be obtained:

$$\omega^2 = gk\tanh(kd) \tag{2.30}$$

The linear dispersion relation connects the wave frequency (or wave period) to the wave number (or wavelength), coupling the temporal and spatial dynamics of the wave evolution. When the dispersion relation is combined with the wave velocity, or phase speed, the following is obtained:

$$c = \frac{\lambda}{T} = \frac{\omega}{k} = \sqrt{\frac{g}{k}\tanh(kd)} \tag{2.31}$$

This formula indicates that the wave speed is a function of the wave number and consequently the wave frequency. As a result, longer waves travel faster than shorter waves. The dispersion relation shows that a combination of wave components of varying frequencies, i.e. a sea state, gradually separates into distinct wave fields, with longer waves moving ahead of the shorter ones. The initially concentrated wave energy disperses throughout the ocean.

2.2.4. Kinematic stretching methods

Stretching methods are widely used in wave kinematics to account for inaccuracies in the prediction of particle velocities and accelerations near the free surface when using linear wave theory. Linear wave theory assumes small wave heights and the boundary conditions are defined at the MSL $z = 0$ and not up to $z = \eta$. This leads to errors in describing the actual movement of water particles near the free-surface. Stretching methods, such as uniform and Wheeler stretching, provide a way to modify the vertical positions of wave kinematics to better reflect the nonlinear wave behaviour. The basic idea is to manipulate the depth decay function $E(z)$, the hyperbolic (co)sine terms in Equation 2.26.

Uniform or vertical stretching adjusts the vertical coordinates of the water particles uniformly based on the instantaneous water surface elevation, effectively "stretching" the water column to reflect the wave motion without changing the overall structure of the velocity profiles:

$$z'(t) = z \cdot \left(1 + \frac{\eta(t)}{d}\right) \tag{2.32}$$

Another commonly applied method is Wheeler stretching. The idea is that the kinematic profile is stretched or compressed to the actual water column height. This is achieved by replacing the original z coordinate in the depth decay function by z', defined as:

$$z'(t) = d\left(\frac{z + \eta(t)}{d + \eta(t)}\right) \quad \text{for} - d < z' < \eta(t) \tag{2.33}$$

Where z is the original vertical depth vector ranging for $z = 0$ at the MSL and $z = -d$ at the seabed, $\eta(t)$ is the free-surface signal and d is the water depth.

Stretching methods offer an improvements to linear wave theory by introducing a first-order approximation of the wave's effect on the kinematics. The method is particularly advantageous because of its simplicity and ease of implementation in numerical models. While stretching methods are widely used, it is important to note that these methods are non-physical approximations. Wheeler pointed out that the Laplace equation (Equation 2.19) is not satisfied and errors might occur when stretching is applied for steep waves.

Nonlinear wave theories, on the other hand, inherently account for variations in wave elevation and the nonlinearities of the free surface, eliminating the need for such corrections. These nonlinear methods will be discussed in the next sections.

2.2.5. Nonlinear wave theory

The linear wave theory that is described in previous section, breaks down when the waves become too steep. Still, when nonlinear effects are weak or only occur intermittently, the global treatment of the waves can still be linear and only nonlinear theory is only required on a local scale. The wave validity graph in Figure 2.5 indicates for which wave height and water depth combination, which theory is recommended. Here, only the theories of Stokes [28] and Dean [31] are discussed as these are appropriate for steep waves. Cnoidal theory [32] is applicable for shallow water only. The main improvement compared to linear wave theory is that the small wave amplitude assumption is relaxed. Stokes wave and Dean stream function theory can be classified as perturbation methods. Both add extra harmonics to the basic harmonic from linear theory, accounting for nonlinear effects. Both theories are similar but where Stokes theory is formulated in terms of the velocity potential and corrections are obtained successively, Dean's theory is based on the stream function and corrections are obtained simultaneously.

Other effective approaches to obtain nonlinear kinematics are based on partial differential equations that can be solved numerically. One numerical method in particular will be discussed in section 2.4. Before moving on, it is essential to highlight another key motivation for studying nonlinear kinematics: the phenomenon of breaking waves.

2.3. Wave breaking

Wave breaking plays a crucial role in the dissipation of wave energy, generating turbulence and potentially imposing significant loads on offshore structures. Accurately representing wave breaking in numerical models presents a challenge due to the complex dynamics involved. The following sections will first discuss the mechanisms and causes of wave breaking, followed by an overview of common modelling approaches.

2.3.1. Breaking wave mechanics

The primary cause of wave breaking is when the wave becomes too steep. Wave steepening can be caused by several aspects, such as a (sudden) change in water depth, a strong opposing current, wind energy transfer to the water surface or nonlinear wave-wave interactions.

A specific case of depth-induced wave breaking or shoaling can be easily observed along the shorelines. The shallow water wave celerity, approximated by $c = \sqrt{gd}$, is almost exclusively due to water depth. In shallow water, the orbital motion of the particles at the base is flattened and becomes more elliptical, see Figure 2.4. The velocities at the bottom decreases due to bottom friction. The particle velocities at the crest are higher, causing the crest to overtake the base resulting in a steep wave front that eventually collapses. For deep waters, the waves are more dispersive, meaning that waves with different wavelengths travel at different speeds. Hence, the intermediate or deep water wave celerity also depends on the wavelength. However, when the water depth suddenly changes, due to the presence of a sandbank for example, the wave celerity also decreases causing wave energy to concentrate, increasing the wave height and steepness which can potentially result in wave breaking.

A strong opposing current can also cause wave breaking. As the wave propagates against the current, the relative velocity between the wave and the water increases. This compresses the wavelength and increases the wave steepness, eventually causing the wave to break. Wind-induced breaking, also known as whitecapping, occurs when the wind transfers energy to the water surface, creating small-scale turbulence and instability. When the wind is strong enough, it can cause the crests of waves to become unstable and break, even if the wave is not overly steep. This process forms white caps, which are common in open seas during storms or windy conditions. During storms, wave heights can increase significantly due to the transfer of energy from the wind to the water surface. While the wavelength tends to remain relatively constant, the increased wave height results in greater wave steepness, leading to wave breaking. In certain cases, nonlinear interactions between waves can lead unusually large waves, known as rogue waves, in a group of waves. Energy can be transferred from smaller waves to larger ones, causing these waves to steepen rapidly. Even in deep water, this steepening can result in breaking if the wave grows too large relative to its wavelength.

Thus, when waves become too steep, they reach a point where they can no longer maintain a stable form, leading to wave breaking, either a spilling breaker or a plunging breaker. In a spilling breaker, the wave crest gently collapses, and turbulence forms at the surface as the wave loses energy gradually. In a plunging breaker, the crest overturns and crashes down, creating a strong turbulent zone. In both cases, the breaking process generates significant turbulence along the front face of the wave, resulting in energy dissipation. The turbulent motion redistributes the kinetic energy into smaller scales, where viscous forces convert it into heat. Additionally, energy is lost in the form of sound and other secondary effects, such as the entrainment of air and the generation of bubbles.

2.3.2. Modelling methods

Only advanced models such as CFD are able to capture these wave breaking processes. The industry practice for offshore structure design relies often on (extended) linear wave theory. Linear (or weakly nonlinear) wave models cannot model the onset of wave breaking. These theories require the waves to be symmetric with respect to the vertical axis and wave steepening cannot be captured. To still provide estimations for wave breaking loads, often an extra forcing term is added to compensate for lack of the breaking wave behaviour in the wave kinematics. This engineering solution is often employed by designers and can be quite effective [7], [33]. These wave breaking or slamming models are discussed in subsection 2.5.4. Since the waves do not actually break, a breaking criteria is required. Many parameters are important for wave breaking, such as the water depth, wave height and length before breaking, steepness and seabed slope. Several formulas exist to describe wave breaking criteria. Robertson et al. [34] reviewed many of the relationships and concluded that one single formula for all conditions is still elusive.

The design standards propose several limits. For example, the wave breaking limit for shallow water, depth-induced, is when the wave height becomes approximately 78% of the local water depth ($H_b = 0.78d$), where H_b is the breaking wave height [17]. The steepness-induced limit is:

$$H_b = 0.142\lambda_b \tanh\left(\frac{2\pi d}{\lambda_b}\right) \tag{2.34}$$

Where λ_b is the breaking wavelength and d is the water depth [18]. The breaking limit for deep water is when the wave steepness (H_b/λ_b) exceeds 1/7 but can be as low as 0.55 under idealized conditions [17], [18]. A more accurate breaking wave height limit is proposed in the DNVGL-PR-C205 given by Goda [35]:

$$H_b = A\lambda_0 \left[1 - \exp\left(-1.5\pi \frac{d}{\lambda_0}\left(1 + 11(\tan\theta)^{4/3}\right)\right)\right] \tag{2.35}$$

Where $A = 0.12 - 0.18$ is a coefficient (0.17 is recommended), $\lambda_0 = (g/2\pi)T_b^2$ is the deep water wavelength, T_b is the period of the breaking wave and θ is the sea floor slope.

Nonlinear wave models offer a more accurate representation of the actual wave breaking behaviour. Part of the actual wave breaking behaviour can be included in the wave model and the wave kinematics. Still, the process is simplified, single-valued models cannot capture overturning waves. However, often closure models are implemented so that the global properties of wave breaking can be obtained.

One common approach is to use energy dissipation models that rely on parametrizations, such as the Battjes and Janssen [36] model. This model approximates the energy dissipation due to wave breaking by introducing empirical parameters such as wave height, breaking probability, and energy dissipation rates. These models simplify the complex physics of wave breaking by using statistical relationships to describe the probability of waves breaking and the associated energy loss. Another commonly employed parametrization is Thornton and Guza [37], which relates energy dissipation to wave height and breaking frequency, but also relies on empirical relationships and parameters. In contrast, SWASH does not use a parametrization for wave breaking. Instead, it models wave breaking through a more direct numerical approach, treating it as a hydraulic jump or bore. This approach captures the breaking process more accurately without relying on predefined parameters, and will be discussed further in subsection 2.4.3. However, air-entrainment, overturning and wave breaking turbulence is not captured.

2.4. SWASH

The nonlinear kinematic model of choice is SWASH, developed by Zijlema et al. [26]. SWASH is an acronym for Simulating WAves to SHore and is a non-hydrostatic fluid flow model originally designed for coastal water applications. Unlike hydrostatic models, SWASH relaxes the assumption of hydrostatic pressure by incorporating vertical accelerations directly into the governing equations, enabling a more accurate representation of wave dynamics, particularly in nonlinear and steep wave conditions.

The ability to account for vertical accelerations is critical in capturing the processes leading up to wave breaking, where steepening and nonlinearity, discussed in subsection 2.2.5, are relevant. For short or steep waves, the inclusion of vertical accelerations provides a more precise description of wave transformation and breaking, compared to models that neglect these effects. This makes SWASH particularly well-suited for applications requiring the accurate simulation of nonlinear wave phenomena.

2.4.1. Governing equations

The governing equations are based on the Euler equations for incompressible fluids. Although SWASH can be used for 3D applications, unidirectional waves are assumed during this project, simplifying the domain to only one horizontal and the vertical dimension. the 2D-vertical domain governing equations (Euler equations) will be presented below:

$$\nabla \cdot \boldsymbol{u} = \frac{\partial u_x}{\partial x} + \frac{\partial u_z}{\partial z} = 0 \tag{2.36}$$

$$\frac{\partial u_x}{\partial t} + \frac{\partial u_x u_x}{\partial x} + \frac{\partial u_x u_z}{\partial z} + \frac{\partial P}{\partial x} = 0 \tag{2.37}$$

$$\frac{\partial u_z}{\partial t} + \frac{\partial u_x u_z}{\partial x} + \frac{\partial u_z u_z}{\partial z} + \frac{\partial P}{\partial z} = -g \tag{2.38}$$

The fluid is assumed to be incompressible with constant density ρ_0 and the vertical domain ranges from the free-surface $z = \eta$ to the seafloor at $z = -d$. $\boldsymbol{u}$ is the fluid velocity vector, with a horizontal and vertical component, u_x and u_z respectively, g is the acceleration due to gravity. The Euler equations assume that the fluid is in-viscid and turbulence modelling is omitted. SWASH can also utilize the Reynolds-Averaged Navier-Stokes (RANS) equations with a turbulence model, such as the $k-\epsilon$ model is possible [26]. P is the total pressure, normalised with the reference density ρ_0, defined as follows:

$$P = p - gz = q + g(\eta - z) \tag{2.39}$$

Where η is the free-surface elevation, p and q are the dynamic and non-hydrostatic pressures, respectively. The non-hydrostatic pressure at the free-surface $q|_{z=\eta} = 0$ as surface tension is neglected. The kinematic boundary conditions at the free-surface and impermeable seafloor with zero slope:

$$u_z = \frac{\partial \eta}{\partial t} + u_x \frac{\partial \eta}{\partial x} \quad \text{at} \quad z = \eta \tag{2.40}$$

$$u_z = 0 \quad \text{at} \quad z = -d \tag{2.41}$$

The free-surface equation can be obtained by integrating Equation 2.36 over the water column $h = d + \eta$ and applying the kinematic boundary conditions:

$$\frac{\partial \eta}{\partial t} + \frac{\partial}{\partial x} \int_{-d}^{\eta} u_x dz = 0 \tag{2.42}$$

The horizontal grid can either be unstructured, orthogonal structured or, for this project, rectilinear structured [38]. The vertical grid is split into a fixed number of equidistant layers. The non-hydrostatic pressure can be arranged with a central difference scheme or with a Keller-Box scheme where the pressure is defined at the cell face. According to Zijlema and Stelling [39], the Keller-Box scheme is more robust and and therefore preferable. For the derivation of the layer-integrated governing equations for a system of any numbered of vertical layers the reader is referred to Zijlema and Stelling [40].

2.4.2. Inflow and outflow conditions

the open boundary inflow condition has many options. For the sake of brevity, only the relevant wave generation inflow and outflow conditions will be discussed. The outflow boundary has the same water depth as the inflow and therefore a simple absorption condition will suffice. A sponge layer can be defined that fully absorbs the waves, given that the layer has sufficient length. Regular waves can be generated by introducing an amplitude, frequency and optionally a phase angle. The incident free-surface signal is then:

$$\eta_b = a_0 + a\cos(2\pi f t + \varphi) \tag{2.43}$$

Where a_0 is the amplitude of the zero frequency, a the main amplitude, f the frequency and φ the phase angle. For unidirectional irregular waves, linear theory is applied and the the inflow target velocity $u_{x,t}$ is defined as a superposition of N harmonic waves. Either, a variance density spectrum is sampled with a random phase for each realisation or externally obtained Fourier components can be used:

$$u_{x,t}(z,t) = \sum_{i=1}^{N} a_i \left[\omega_i \frac{\cosh k_i(z+d)}{\sinh k_i h} + \sqrt{\frac{g}{h}} \right] \cos\left(2\pi f_i - \varphi_i\right) - \sqrt{\frac{g}{h}}\eta \tag{2.44}$$

Where a_i, k_i and φ_i are the amplitude, wave number and phase angle of each frequency component f_i. When phase angles are randomly sampled, a uniform distribution is assumed between 0 and 2π. The spectrum can be specified through a parametric shape, such as the JONSWAP spectrum. To counter reflections at the wave maker boundary, a weakly reflective condition can be applied. The total inflow velocity is then a superposition of the target velocity $u_{x,t}$ and the velocity of the reflected waves $u_{x,r}$, i.e. $u_x = u_{x,t} + u_{x,r}$. The reflected waves are assumed to be shallow water waves and the condition read as follows [41]:

$$u_{x,r} = \sqrt{\frac{c}{h}}(2\eta_w - \eta) \tag{2.45}$$

Where subscript w indicates the wave maker boundary, located at the west side of the domain, $c = \sqrt{gd}$ is the shallow water wave celerity and $h = \eta + d$ is total height of the water column. When dealing with high waves, nonlinear triad wave interactions arise. The interactions between three wave components generate additional wave components at sub-harmonic, infragravity waves, and super-harmonic frequencies. These components, known as bound waves, are bound to the primary wave and have the same group velocity, meaning they move with the primary wave instead of travelling at their own natural speed based on their wavelength. Bound waves arise from the energy exchange between interacting wave frequencies and are essential for nonlinear wave theory.

Linear boundary conditions cannot account for these bound waves. To match the linear waves generated at the boundary with the desired nonlinear target wave conditions, spurious waves are generated [42], [43]. These spurious waves have the same magnitude as the bound waves with a 180° phase difference. The problem is that these spurious waves behave like free waves, travelling at their own speed dictated by their own frequency, which is different from the primary wave. These spurious waves cause errors in the simulation. Uneven and spatially varying wave fields arise where wave heights fluctuate across the domain.

To resolve this issue and ensure a more realistic wave simulation, second-order bound waves at the wave maker boundary can be introduced. By explicitly generating the second-order sum and difference components, representing the super-harmonic and sub-harmonic bound waves, at the boundary, the spurious waves can be significantly eliminated provided that the wave maker is placed at an appropriate depth. Rijnsdorp et al. [41] introduced a method to incorporate the second order sub-harmonics or infragravity waves into the target inflow velocity condition. Vasarmidis et al. [44] derived an exact mathematical solution that includes both sub- and super-harmonic second-order components in the wave generation process. The reader is referred to that article for a detailed derivation and further explanation [44]. It must be noted that latter method is only applicable for a vertical resolution up to four layers.

2.4.3. Wave breaking

As briefly mentioned in subsection 2.3.2, wave breaking is represented using a numerical approach rather than a parametrization. The model draws an analogy between a breaking wave and a hydraulic jump or bore [45], where momentum conservation is enforced across the discontinuity at the wave front. By conserving momentum in this manner, the energy dissipation rate becomes proportional to the cube of the wave height (H^3), mirroring the dissipation observed in hydraulic jumps [46]. This approach simplifies the computational process while effectively capturing the bulk characteristics of a breaking wave without resolving the detailed turbulence.

In SWASH, wave breaking is treated as a sub-grid phenomenon, where the flow field in the entire water column below the turbulent front is considered at a scale smaller than the grid size. Processes such as turbulence, air entrainment, and wave overturning are not explicitly resolved. Instead, the model focuses on momentum conservation and energy dissipation, capturing the bulk effects of wave breaking. As wave steepness increases, the forward pitching can become unstable (spilling breakers) or overturns (plunging breakers), creating a turbulent front. In reality, the turbulent motions generated during breaking play a stabilizing role by transporting momentum downward, helping to stabilize the bore front and establish a quasi-steady bore [47]. However, in SWASH, these turbulent motions are not modelled, so the steepness continues to increase until the transition from wave trough to crest can no longer be resolved. A jump-discontinuity (a sudden, sharp change in water surface elevation and velocity) forms, with a jump height equal to the local wave height. After the jump-discontinuity forms, the model enforces momentum conservation across the discontinuity, ensuring that the flow conditions before and after the jump remain balanced in terms of momentum transfer. At the same time, energy is dissipated to represent the loss associated with wave breaking.

To properly simulate this discontinuity and the dynamics of the breaking process, the model requires high vertical (and horizontal) resolution to accurately represent the sharp changes in water surface elevation and velocity. Although this approach allows SWASH to represent the bulk effects of wave breaking (such as momentum transfer and energy dissipation) efficiently, it does not resolve the small-scale turbulence and vortex generation that occur during breaking. This trade-off can lead to overestimation of local wave kinematics, especially near the wave crest, due to the absence of turbulence effects and the damping influence of air entrainment.

Now that all the relevant kinematic models are discussed, the transition can be made to the hydrodynamic loads.

2.5. Hydrodynamic loads

Hydrodynamic forces acting on offshore wind turbine monopiles are a critical aspect of structural design. These forces are primarily transmitted through the structure to the seabed as shear forces and bending moments. This section will discuss methods to obtain the hydrodynamic loads from wave kinematics. The focus will be on determining the inline forces on a monopile support structure. The most common method is the semi-empirical Morison equation.

2.5.1. The Morison equation

Morison et al. [22] originally derived this method for calculating wave loads on fixed vertical cylinders. The formulation is based on the assumption that the structure is slender, relative to the wavelength. The method is based on the observation that the force has two main components. One component is related to the fluid particle acceleration, the fluid inertia force, and the other is related to the velocity, the drag force. The original formulation is as follows:

$$f(z,t) = C_M\left(\rho\frac{\pi D^2}{4}\right)a_x + C_D\frac{\rho D}{2}|u_x|u_x \tag{2.46}$$

Where $f(z,t)$ is the distributed fluid force per unit length on the structure, D is the pile diameter, ρi is the water density, C_M and C_D are the coefficients of mass and drag and $a_x = \partial u/\partial x$ and u_x are the horizontal fluid particle acceleration and velocity, respectively that both depend on the vertical coordinate z and time t.

$f(z,t)$ must be integrated over the depth to obtain the total shear force in time. When the distributed force is multiplied with the point of application and then integrated, the overturning moment is obtained:

$$F_{shear}(t) = \int_{-d}^{\eta} f(z,t)dz \tag{2.47}$$

$$M_{ovt.}(t) = \int_{-d}^{\eta} f(z,t)\cdot z dz \tag{2.48}$$

Depending on the dimensions of the structure and the wave conditions, the drag and inertia component vary in significance. The Keulegan-Carpenter number (KC) [48] can be used to find the relative importance of the drag and inertia force in oscillatory flow. It is defined as the ratio of the maximum horizontal displacement of fluid particles to the characteristic dimension:

$$KC = \frac{u_{x,m} T}{D} \tag{2.49}$$

Where $u_{x,m}$ is the maximum particle velocity, T is the wave period and D is the characteristic dimension, the pile diameter in this case. For $KC < 5$ the flow can be assumed to be inertia dominated and for $KC > 20$ the flow is drag dominated. For $5 < KC < 20$, both inertia and drag components are significant. Figure 2.6 visualises for which dimensionless pile diameter $\pi D/\lambda$ and wave height H/D the inertia, drag and or diffraction components are relevant.

Experiments have indicated that for the intermediate regime, it is more difficult to estimate the force with the Morison equation [49]. The drag and inertia component can have an influence on each other, making the linear superposition of both components inaccurate. Furthermore, complex flow phenomena, like vortex shedding and flow separation may occur around the structure which is neglected. These effects introduce nonlinearities that are not captured by the Morison equation. Finally, for highly nonlinear wave conditions, such as extreme waves, the velocity and acceleration fields are more complex, and linear assumptions about wave kinematics can lead to errors in estimating forces using the Morison equation.

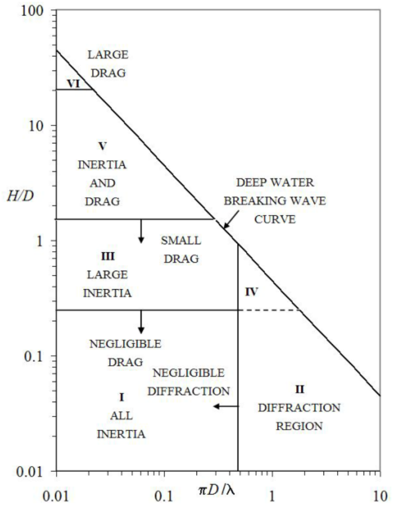

Figure 2.6: Wave force regimes based on dimensionless wave height and slenderness ratio [5].

Slamming forces, which occur when breaking waves or steep waves impact the structure, generating intense, short-duration forces that can be as much as 2.8 times larger than the forces from non-breaking wave loads [6]. To accurately account for slamming forces, it is crucial to incorporate the nonlinear behavior of breaking waves. This can be done either by applying nonlinear wave kinematics to model the wave's interaction with the structure or by using a dedicated slamming model designed to capture the rapid pressure rise and intense forces associated with wave impact.

Slamming models provide a more focused approach to handle the complex force dynamics generated by these extreme wave events, as they explicitly address the impact mechanism that occurs when the wave crest collides with the structure. These models will be further discussed in subsection 2.5.4.

2.5.2. Morison coefficients

Although the Morison equation is often described with two components, it is actually a combination of three components. The inertia term consists of a contribution due to the pressure field generated by the incident wave, the Froude-Krilov force and a contribution due to the inertia of the surrounding fluid that must be accelerated, the so-called added mass. These components both depend on the total fluid mass $\rho\pi D^2/4$ and the particle acceleration and are therefore often combined. The theoretical C_M for a smooth cylinder in potential flow is 2, where the coefficient from the undisturbed flow, the Froude-Krilov component is 1 and the coefficient for the disturbed flow due to the cylinder, C_a, is also 1. In practice, the Froude-Krilov component can be safely assumed to be 1. The added mass coefficient C_a is usually smaller than 1. The mass or inertia coefficient can thus also be written as $C_M = 1 + C_a$, where C_a is the added mass coefficient. The drag and inertia coefficient C_D and C_M depends different parameters, such as the Keulegan-Carptenter number, the Reynolds number and surface roughness. The coefficients can be determined empirically or with analytical methods. However, it is common practice during the design phase to assume $C_D = 0.9$ and $C_M = 2.0$ [18].

2.5.3. Slamming Detection

Breaking waves are not necessarily the largest waves in terms of height, making them harder to identify based on wave elevation alone. Without the spatial evolution of the waves at the structure, detecting slamming events based purely on wave height can lead to inaccurate results. Therefore, it is crucial to use additional indicators beyond wave elevation to accurately identify slamming events. An intuitive method is visual detection of slamming events during physical experiments. This can be effective for small-scale tests or short-duration experiments where wave breaking is visible, but it becomes impractical for long-duration experiments or numerical simulations involving extended time series. Given the limitations of visual observation, automated or data-driven methods are necessary for reliably detecting slamming forces over longer periods or in more complex wave environments.

When time series data of wave-induced forces are available, there are additional methods for detecting slamming events based on the force signal itself. Two approaches will be discussed from scientific articles that developed slamming models. In the paper by Paulsen et al. (2019) [7], a method is proposed based on two main criteria for detecting slamming events from the force time series. Their definition of a slamming event is:

> *a significant load increase over a time interval significantly shorter than the time scales associated with the incident waves.*

The criteria read as follows:

1. The duration of the slamming event τ_b must be much shorter than the peak period T_p, more specifically $\tau_b \leq 0.125 T_p$
2. The peak slamming force $F_b(t)$ should exceed three times the standard deviation of the force time series, .e. $F_b(t) \geq 3\text{std}(F(t) - \bar{F(t)})$

The first criterion ensures that the slamming duration is brief relative to the dominant wave period, while the second ensures that the slamming force is significantly higher than the typical wave-induced forces.

2.5.4. Slamming models

The first wave impact on cylinder model was proposed by Goda [35] to estimate the force on seaplane floats during landing. Based on the 2D impact model of von Kármán [50] which is derived from momentum theory, the overall loading is assumed to be driven by the added mass effect. The impact force is expressed as:

$$F_s(t) = \kappa \eta_b \rho R c^2 C_s \tag{2.50}$$

$$C_s = \pi \left(1 - \frac{u}{R} t\right) \tag{2.51}$$

Where κ is the curling factor, representing the fraction of the wave crest that is assumed vertical and causing the slamming impact and η_b is the breaking wave surface elevation, so $\kappa\eta_b$ is the height of the impact area, see Figure 2.7 for reference. R is the cylinder radius, c is the wave celerity and C_s is the slamming coefficient.

This model, however, neglects the pile-up effect, which was later addressed by Wagner's theory [51]. using potential flow. Wagner found that the maximum impact force occurred with a slamming coefficient $C_s = 2\pi$. Further research aimed at refining the slamming coefficient led Campbell and Weynberg [52] propose a semi-empirical formulation for C_s:

$$C_s = 5.15\left(\frac{D}{D+19u_x t} + \frac{0.106u_x t}{D}\right) \tag{2.52}$$

Where u_x is the horizontal velocity of the water particles, t is the time after the initial wave impact and D is the pile diameter.

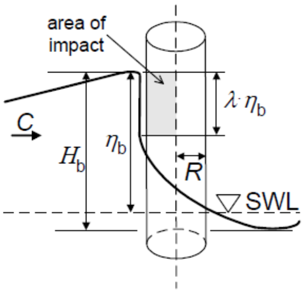

Figure 2.7: Sketch of the breaking wave impact force on a vertical cylinder [6]

Wienke and Oumeraci [6] conducted a comprehensive experimental study to improve slamming load models. They built upon Wagner's theory by including the effects of pile-up and radial spreading of water, which significantly influence the slamming loads. Their method is widely accepted and implemented in design guidelines, including those from IEC 61400-3 [17] and DNV [18].

Paulsen et al. (2019) developed a more refined approach for modelling slamming forces on offshore structures. The distributed slamming force f_s must be included as an additional term to the Morison equation. When a breaking wave event is identified with a certain breaking wave height H_b, the formulation according to Paulsen et al. [7] is:

$$f_s(z',t) = \frac{1}{2}\rho c^2 C_s g(t) G_y(z') D \tag{2.53}$$

Where the wave speed can be estimated with the shallow water approximation $c = \sqrt{gd}$, the slamming coefficient can be assumed $C_s = 2\pi$ for cylinders with pile diameter D. Temporal and spatial distributions, $g(t)$ and $G_y(z')$ respectively, have been empirically developed. The temporal development is modelled by a squared sine wave as:

$$g(t) = \sin^2\left(\pi\frac{t}{T_s}\right) \quad \text{for} \quad 0 < t < T_s \tag{2.54}$$

$$T_s = \frac{13D}{32c} \tag{2.55}$$

Where T_s is the duration of the impact event. The breaking wave period T_b can be estimated with $T_b = 0.9T_p$, where T_p is the peak wave period. The non-dimensional vertical spatial distribution based on the relative elevation coordinate z', integrated over the pile width, is:

$$G_y(z') = \frac{4-8|z'|}{\pi^2} \tag{2.56}$$

$$z' = \frac{z-\eta_b}{\kappa H_b} \quad \text{for} \quad 0.5 < z' < 0.5 \tag{2.57}$$

Where $H_b = 1.4H_s$ is the breaking wave height and H_s is the significant wave height. The distributed slam force f_s is applied over the the height of the impact area, $\kappa\eta_b$, where the curling factor defined as:

$$\kappa = 0.29\frac{H_b}{H_s} \tag{2.58}$$

3

Methodology

To achieve the research objective, the nonlinear wave model must be both validated and compared to existing methods. Available experimental data will be used in this validation process, providing a reliable basis to test the accuracy of the model. Additionally, comparing the nonlinear model to a linear, industry-standard model allows for a better understanding of the differences in performance. The linear model serves as a benchmark, offering a reference for how much improvement is achieved by the nonlinear approach.

This chapter will discuss the data sources and numerical models that are used during this project and their implementation. The experimental data was readily available and is thoroughly described in section 3.1. The implementation of linear wave theory is discussed in subsection 3.2.1. Implementation of the non-hydrostatic wave model SWASH is provided in subsection 3.2.2 and the application of the Morison equation for both SWASH and the linear wave model in section 3.3.

3.1. Experimental data

To validate the numerical models and evaluate their performance, a comparison is made with experimental data. One of the objectives of this research project is to deterministically compare experimental and numerical time series. As the experiments were already performed, the experimental setup will be replicated in the numerical models. Therefore, a detailed description of the setup will be provided in this section.

The available datasets were measurements from an experimental campaign that was part of a Joint Industry Project called "Wave Impact on Fixed structures"(WIFI) [53]. As the name states, the purpose was to extend the knowledge regarding extreme and breaking wave impact loads on offshore wind turbine support structures. The experiments were conducted in the Atlantic Basin at Deltares, Delft. 50-year return period storm waves were generated that propagated over some distance towards a target location where two different sized monopiles were installed. The experimental campaign was extensive and many tests were performed with different setups. For this project only the reference setup results were used.

3.1.1. Experimental setup

The length scale factor that is deployed is 1:45 and Froude scaling is applied. The reference setup is a flat sea floor without current. The wave basin is 75 meters long, 8.7 meters wide and a maximum water depth of 1 meter. At one end, at some distance from the basin wall, a wave maker generates waves that propagate through the basin to the other end. At the target location, approximately 31 meters from the wave maker, two monopiles were installed at equal distance from the centre. The diameters are 0.1 and 0.16 m at model scale. These correspond to full-scale diameters of 4.5 and 7.2 m, respectively. Only the force and moment measurements on the largest diameter monopile are used as the largest diameter is most relevant for current generation wind turbines.

To overcome wave reflections that contaminate the measurements, an artificial beach is located on the right side of the domain. The wave maker itself is equipped with Active Reflection Compensation (ARC) [7]. ARC reduces the reflected waves from the left side boundaries by detecting them and generating compensating counter waves to cancel them out. Full absorption is not achieved but the reflections are assumed to be negligible. Furthermore, the wave maker is able to generate second order waves, limiting the generation of spurious waves.

3.1.2. Test conditions

Both regular and irregular long crested waves were generated. Long crested means that the waves travel in one direction along the basin with the wave crest as wide as the basin width. The results can therefore be interpreted in two dimensions, one horizontal direction and the vertical direction. This allows the numerical models to be deployed in 2D as well, resulting in less computational cost.

The regular wave tests were used solely to validate the nonlinear wave model, while the measurements from the irregular wave tests served as the primary data for this project. Only short duration regular wave realisations were required as all waves have one amplitude and frequency, provided in Table 3.1, and cause the same loading on the structure. Five irregular wave experiments of approximately 1000 waves were conducted per setup with different phase angle seeds to obtain unique results. The wave design conditions were chosen as being typical for the North Sea storm with a return period of 50 years. Irregular waves were generated with the JONSWAP spectrum as input, with peakedness of $\gamma = 3.3$ and the significant wave height and peak period from Table 3.1.

Table 3.1: Targeted input conditions for regular and irregular wave experiments, full and model scale [7].

		Full scale	Model scale
depth d	[m]	30	0.67
(significant) wave height H or H_s	[m]	10	0.22
(peak) wave period T or T_p	[s]	13	1.94

3.1.3. Measurements

The free-surface elevation is measured by 11 wave gauges, distributed through the basin. A schematic overview of the experimental setup is given in Figure 3.1. Similar wave gauge sensor numbering will be used in the numerical models. Most of the measurements that are used will be from the sensors placed in the centre of the basin ($y = 0$ m) and results will always be presented in order from the wave maker (at $x = 0$ m) to the artificial beach at (starting from $x = 50$ m).

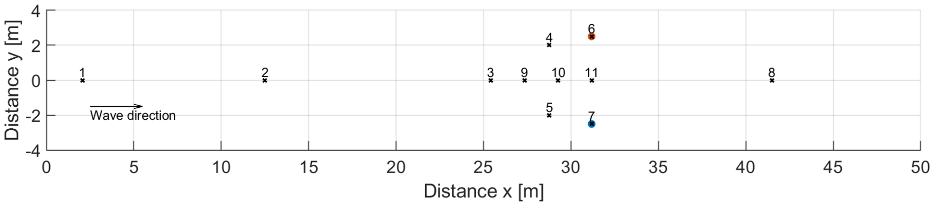

Figure 3.1: Schematic overview of the experimental setup with the wave gauge sensors. The wave maker is located at x = 0, the orange dot is cylinder 1 (D = 0.1 m) and the blue dot is cylinder 2 (D = 0.16 m).

Force transducers were installed at the top and bottom of the piles to measure the hydrodynamic loads in terms of total shear force and overturning moment. The bottom force transducer is placed below the seafloor to overcome interference. Hence, the moment measurements are not exactly the overturning moment at the mudline which must be taken into account when the moments are compared with the numerical models.

The piles were installed with rigid connection. The goal of the experiments was to measure the force acting on the structure and not the response. However, some movement was required to measure the strain and determine the force. As a result, the system could be excited at its natural frequency that was determined to be 80 Hz. Especially during violent impact, waves breaking on the structure, excitation occurred at the natural frequency. The force measurements were therefore filtered to remove the pile response from the force measurements. The fact that the measurements were filtered in this manner is important to keep in mind during the analysis. The sampling frequency was 1000 Hz for all sensors.

3.2. Wave kinematics

This section will describe the implementation of the linear and nonlinear model to obtain the wave kinematics. For a theoretical discussion about the underlying equations, the reader is referred to subsection 2.2.3 and 2.4. First, both models are compared against the measured data. For a deterministic comparison in the time domain, a reconstruction of the free-surface elevation from the experimental measurements is required. This can be achieved by using the Fourier series, obtained from a Fast Fourier Transform (FFT) on the free-surface signal from the measurements (subsection 2.1.3). The Fourier series represent the exact wave spectrum observed in the experiments, with the correct phase angles that reflect the specific interactions and wave patterns measured in the laboratory. By prescribing the Fourier series at the inflow boundary in SWASH, waves are generated that propagate through the numerical domain. The linear wave model transforms the Fourier series to kinematic components that can be superimposed to obtain the linear kinematics.

Free-surface measurements are not available during the design phase of offshore wind turbine. Instead, random sea states are obtained with the random phase/amplitude model, see subsection 2.1.2. A wave spectrum can be defined with spectrum shape and the bulk wave parameters, significant wave height and peak period. The wave components can then be derived from the spectrum, random phase angles are assigned and a free-surface time signal can be obtained. The results can be compared on a statistical level with the measurements rather than deterministically. In the following two sections, the implementation of the linear wave model and SWASH will be described to obtain the free-surface elevation time series and the wave kinematics. Both input methods, based on the Fourier series and bulk wave parameters, will be discussed.

3.2.1. Linear wave theory

Obtaining linear wave kinematics is relatively straight forward. The Fourier series from the wave gauge measurements or wave components from the random phase/amplitude model will be used for the linear model. Then, the superposition principle will be utilized to obtain the particle velocity and acceleration. Recall the acceleration and velocity formulations, Equation 2.26 and 2.28, but now as a superposition of N components:

$$u(x,z,t) = \sum_{i=1}^{N} a_i \omega_i k_i \cdot E1_i(z) \cdot \sin(k_i x - \omega_i t + \varphi_i) \tag{3.1}$$

$$a_x(x,z,t) = \sum_{i=1}^{N} a_i \omega_i^2 k_i \cdot E1_i(z) \cdot \cos(k_i x - \omega_i t + \varphi_i) \tag{3.2}$$

$$E1_i(z) = \frac{\cosh(k_i(d+z))}{\sinh(k_i d)} \tag{3.3}$$

$$w(x,z,t) = \sum_{i=1}^{N} a_i \omega_i k_i \cdot E2_i(z) \cdot \cos(k_i x - \omega_i t + \varphi_i) \tag{3.4}$$

$$a_z(x,z,t) = \sum_{i=1}^{N} a_i \omega_i^2 k_i \cdot E2_i(z) \cdot \sin(k_i x - \omega_i t + \varphi_i) \tag{3.5}$$

$$E2_i(z) = \frac{\sinh(k_i(d+z))}{\sinh(k_i d)} \tag{3.6}$$

(3.7)

When the measurements from the wave gauge sensor at the monopile location are used, sensor 11 see Figure 3.1, the kx term can be omitted as the reference location is at $x = 0$. Otherwise, x denotes the distance in meters from the wave maker or wave gauge sensor the desired location. Although waves are assumed linear, the FFT-based input allows for the retention of some degree of nonlinear wave behaviour. This is because the Fourier series, derived from the experimental measurements, inherently contain the phase coupling between wave components that results from nonlinear interactions. The model is therefore not strictly linear but rather a hybrid model for the Fourier series input.

To consider the wave kinematics above the MSL, a stretching method is required (subsection 2.2.4). Uniform stretching is used due to its simplicity and ease of implementation. z in the depth decay functions $E1_i$ and $E2_i$ is replaced with z':

$$z'(t) = z \cdot \left(1 + \frac{\eta(t)}{d}\right) \tag{3.8}$$

It is important to recognize the spin-up and/or the spin-down phase in the measurement time series and remove them before performing the FFT. The cut-off frequency must be chosen carefully so that most of the wave energy is still present in the input spectrum. In general 4-5 times the peak frequency is enough. Higher frequency components are physically not meaningful and can contain noise. A cut-off frequency of 10 Hz was chosen to ensure a conservative approach. The linear model is not extended with a embedded extreme wave. The purpose of the linear model is to serve as benchmark or comparison method to the nonlinear model. For this reason a simple implementation was chosen.

3.2.2. SWASH

SWASH can be utilized either in one dimensional or two dimensional mode for the horizontal plane. Hence, one dimensional, e.g. 2D-vertical, mode can be used for uni-directional long crested waves, which is a reasonable assumption for the application of this project as the experimental setup also neglects wave directionality. The spatial domain is defined similar to the experimental setup in Figure 3.1. High spatial and temporal resolutions will be deployed to ensure that the simulations converge. When long time series are required, the computational time becomes excessive, up to the point that one simulation requires several days to complete. Parallel computing can be deployed

Initial and boundary conditions

The initial conditions for the velocities and water level are set to zero, which is also the case for the experimental setup. The simulation duration is long enough to achieve steady state solutions. Boundary conditions must be imposed at the boundaries of the computational grid in order to solve the Euler equations. The seabed boundary condition is defined in the computational grid, in this case a seafloor without any slope. At the outflow boundary on the east side, a sponge layer is defined that fully absorbs the wave energy when the sponge layer is sufficiently long, 3 typical wavelengths.

The wave maker is located at the inflow boundary on the west side of the domain. Wave generation in SWASH can be first or second order, see section 2.4. However, the second order method is limited to a vertical resolution of 4 layers. Through the presence of breaking waves, a much finer vertical grid is required and the second order wave generation cannot be deployed. SWASH will therefore deploy the vertical hyperbolic depth decay velocity profile according to linear wave theory (Equation 2.26). The following section will elaborate on wave generation methods that are utilized during this project.

Wave generation

For regular waves, only the amplitude and frequency (or period) need to be defined. In the case of irregular wave generation, various methods can be employed within SWASH. For frequency domain analysis, a JONSWAP wave spectrum (Equation 2.5) is generated using the random phase model based on the bulk wave parameters provided in Table 3.1.

For the deterministic time domain comparison, the Fourier Series will be used as input in SWASH and when the wave maker is moved forward to the location from where the measurements were taken. Wave propagation can be modelled by SWASH and the wave kinematics can be extracted from the monopile location. Applying the force model will retrieve a time series of the forces and moments that can be compared to the experimental force measurements.

Although wave generation in SWASH is linear, in contrast to the second-order wave generation used in the experiments, the FFT-based input allows for the retention of some degree of nonlinear wave behaviour. As stated before in subsection 3.2.1, this is because the Fourier series derived from the experimental measurements inherently contains the phase coupling between wave components that results from nonlinear interactions. As discussed in subsection 2.4.2, for high waves, nonlinear interactions between different wave frequencies generate bound waves at both sum and difference frequencies. These bound waves are phase-coupled to the primary wave components. When the FFT is performed on the experimental data, it captures these nonlinear effects, ensuring the correct phase relationships between the primary waves and their bound wave components. When these Fourier components are used as input into SWASH, the model does not need to explicitly generate the bound waves, as the nonlinear phase coupling is already included in the wave spectrum. Phase coupling results in less significant spurious waves while nonlinearity is preserved to some extent.

Initial resolution

For grid based models such as SWASH, a resolution must be defined. When the resolution is too coarse, the model might not converge or give accurate results but finer resolution are computationally more expensive. Therefore, a grid convergence study is performed, see appendix A. For high waves it is good practice to take at least 100 horizontal grid cells per peak wavelength [54]. This suggestion will be used to estimate the initial horizontal mesh resolution. The wave length can be estimated with the linear dispersion relation, Equation 2.30. The wavelength λ is approximately 4.36 meter for a model scale wave period of 1.94 s, so the initial horizontal grid cell length is 0.04 m. The vertical resolution in SWASH is defined by the number of layers and the choice depends mainly on the type of application and the presence of nonlinearity. As discussed previously, high vertical resolution is required to properly represent wave breaking. Hence, the convergence study for the amount of layers is critical. Additionally, when the number of layers is not sufficient, the high harmonics may propagate too slowly. As an effect, the phase difference between the harmonics will be wrong. When nonlinear effects are present, this is even more important.

Parallel computing

High spatial and temporal resolutions will be used. In the first place to ensure that the simulations converge, but also to completely eliminate grid-induced discrepancies between model and experiments. When long time series are required, the computational time becomes excessive, up to the point that one simulation requires several days to complete. Parallel computing can be deployed for SWASH, with different parallelization strategies. The computing cluster from TU Delft, DelftBlue [55] was therefore utilized to perform complete full duration simulations.

3.3. Hydrodynamic loads

The nonlinear kinematics can now be readily introduced in the Morison equation to obtain the loads (subsection 2.5.1). The wave force regime (Figure 2.6) is on the border of III and V with the slenderness ratio $\pi D/\lambda \approx 0.1$ and dimensionless wave height $H/D = 1.4$ calculated with the peak wavelength of 4.3 m and the significant wave height of 0.22 m. The total load will thus be largely inertia dominated but the drag component cannot be fully neglected. To obtain the drag and inertia components, the corresponding coefficients must be determined. The values for the coefficients are $C_M = 2$, $C_D = 0.9$ according to the recommended design practice [18]. The MacCamy and Fuchs model is not included since the cylinder is slender relative to the wavelength and diffraction can be neglected. The Morison equation can be solved for each discrete layer k in time:

$$f_k(t) = C_M\left(\rho\frac{\pi D^2}{4}\right)a_{xk} + C_D\frac{\rho D}{2}|u_{xk}|u_{xk} \tag{3.9}$$

Where ρ is the water density, D is the pile diameter. The total shear force is obtained by integrating the force components per layer over the total depth. The overturning moment at the mudline is obtained in similar manner by integrating the force components times the point of application of the force with respect to the seabed over the depth.

To quantify and compare the total energy in the force and moment signal and measurements, a similar parameter as the significant wave height H_{m0} (Equation 2.12) can be defined. The significant (shear) force peak and significant (overturning) moment peak are calculated as follows:

$$F_{m0} = 4\sqrt{m_{F,0}} \tag{3.10}$$

$$M_{m0} = 4\sqrt{m_{M,0}} \tag{3.11}$$

Where $m_{F,0}$ and $m_{M,0}$ are the zeroth spectral moments of the force and moment time signals, respectively. With these quantities the global amount of energy can be compared. These quantities can also be used to normalize force or moment peaks.

3.3.1. Linear model application

To further improve the linear hydrodynamic load estimations for extreme events, the slamming model from Paulsen et al. [7] was applied, described in subsection 2.5.4. Only the integrated force and moment over depth are of interest and only the temporal distribution needed to be implemented. The temporal distribution is given in Equation 2.54 and the slam force peak is assumed to coincide with the shear force peak.

3.3.2. Nonlinear model application

The velocities per layer u_{xk} over time can be directly retrieved from the simulation data. Acceleration is computed during post-processing. For the horizontal accelerations a_x, a correction must be applied. Although the amount of layers is equal and the layer thickness is constant over the depth, the output locations of the velocity in horizontal changes over time ($\partial u_x / \partial t$) as the total water depth changes over time ($\partial z / \partial t$). Therefore, the velocities must be corrected. Equation 3.12 calculates the actual water particle accelerations in x-direction a_x independent of the z position:

$$a_x = \frac{\partial u_x}{\partial t} - \frac{\partial u_x}{\partial z}\frac{\partial z}{\partial t} \tag{3.12}$$

4

Validation of the nonlinear model

The first step in evaluating the nonlinear model is its validation. The goal is to demonstrate that the model accurately captures the hydrodynamic loading on the offshore wind turbine support structure. Validation is performed using measurements of the free-surface elevation, shear force, and overturning moment. This chapter presents the validation process and results for the nonlinear wave model SWASH, as well as the implementation of the Morison equation.

4.1. Free-surface validation

The free-surface validation will be performed for setups that increase in complexity. First regular wave results will be presented. Then, the random phase/amplitude model with a significant wave height and peak period will be validated in the frequency domain. Next, Fourier series from the measurements will be used to generate waves. Both frequency and time domain results will be compared to the measurements.

4.1.1. Bulk wave parameter input

Starting with regular waves in Figure 4.1, where the power spectrum density for the experiments and numerical results are visualised. In general, the results agree quite well, especially at the peak frequency 0.5 Hz for the monopile location. The PSD plots for the irregular wave realizations, shown in Figure 4.2, demonstrate a reasonable match between the SWASH simulations and the experimental measurements. A noticeable difference is observed at the peak for the first sensor (sensor 1), where the SWASH simulation underestimates the experimental value. At the target location where the monopiles are installed (sensor 11), the difference in peak energy is smaller.

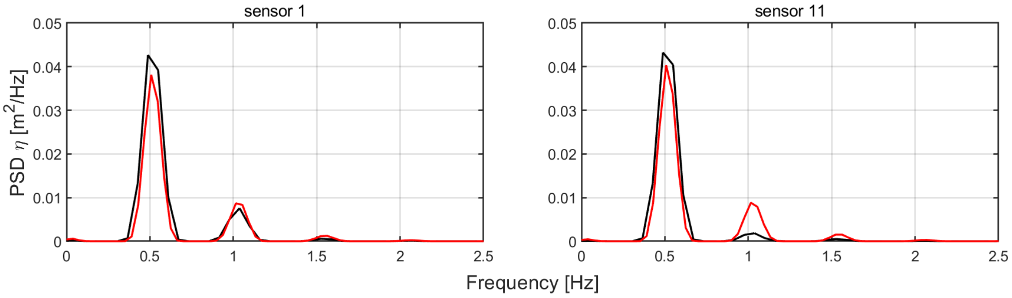

Figure 4.1: Power Spectrum Density plots of the free-surface elevation close to the wave maker, sensor 1 (left) and at the monopile, sensor 11 (right) for SWASH simulation (red) and experimental dataset (black) for regular waves.

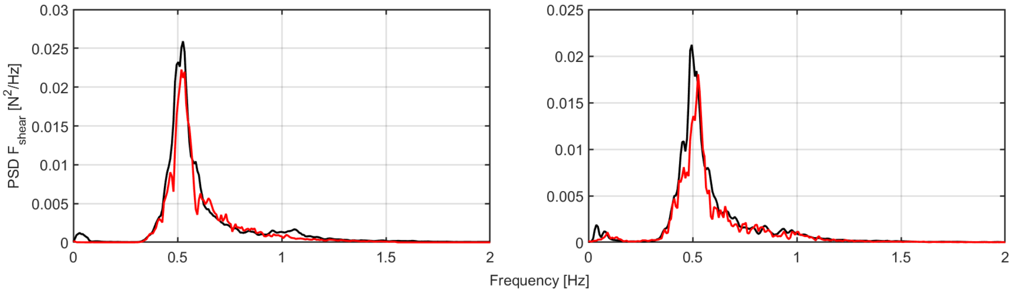

Figure 4.2: Power Spectrum Density plots of the free-surface elevation at the wave maker (left) and monopile (right) for SWASH simulation (red) and experimental dataset (black) for irregular waves.

4.1.2. Fourier input

The Fourier series input method is described in subsection 3.2.2. The PSD of the free-surface elevation at the monopile location is shown on the left side of Figure 4.3, comparing 5 datasets from experimental measurements and 5 corresponding SWASH simulations. While the peak of the SWASH spectrum is slightly lower, the overall spectra demonstrates a good agreement with the experimental data.

On the right side of the same figure, the probability exceedance of normalized wave heights H/H_{m0} derived from a zero-crossing analysis, is presented. The SWASH simulation results exhibit an excellent match with the experimental data, indicating that the SWASH model accurately replicates the statistical distribution of the wave heights.

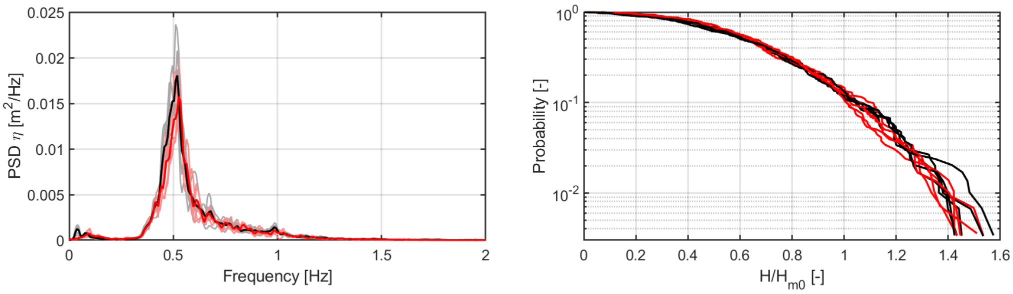

Figure 4.3: Power Spectrum Density of the free-surface elevation (left) and probability exceedance of the wave heights H (right) at the monopile for SWASH simulations (red) with Fourier input and experimental datasets (black).

To further validate the wave elevation, a comparison in the time domain is necessary. To allow for proper wave propagation and evolution of nonlinear effects in the wave model, ideally the wave maker is placed furthest away from the target or monopile location. Therefore, the measurements from the first wave gauge sensor in the experimental setup, sensor 1, were used initially. In Figure 4.4, the time series from the first and target sensors (sensor 1 and sensor 11) are plotted. The signals at sensor 11 are clearly out of phase. A better match is required for further analysis where a deterministic comparison will be made between the signals.

To improve the phase synchronization in the time domain, the position of the numerical wave maker was incrementally moved closer to the monopile. Referring to Figure 3.1, the wave maker was moved to the location of sensor 2, 3, 9 and eventually 10. By shifting the wave maker position upstream, the free-surface signals at the monopile progressively aligned with the experimental data. In the end, the wave maker was placed at the closest sensor, sensor 10 to obtain a reasonable match in the time series of the free-surface, Figure 4.5.

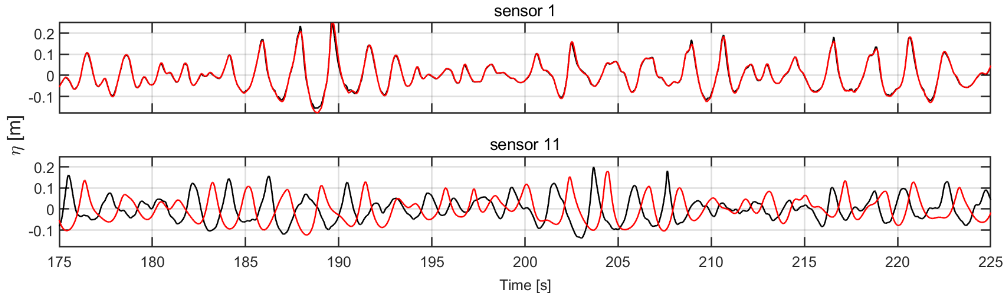

Figure 4.4: Free-surface elevation time series for SWASH simulations (red) with Fourier input from wave gauge sensor 1 and experimental datasets (black).

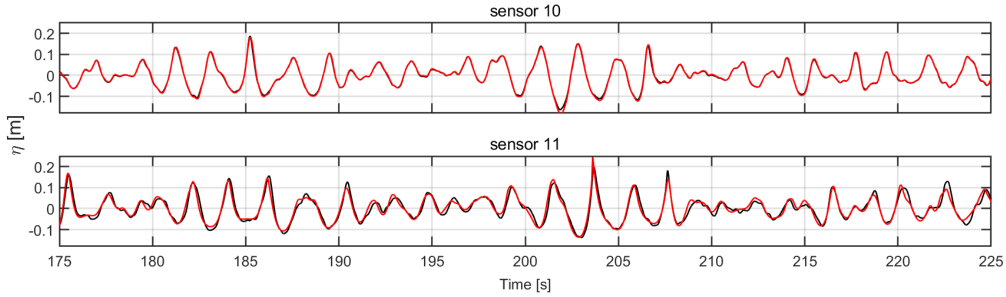

Figure 4.5: Free-surface elevation time series for SWASH simulations (red) with Fourier input from wave gauge sensor 10 and experimental datasets (black).

4.2. Hydrodynamic loads validation

With the nonlinear kinematics, the hydrodynamic loads can be obtained. The results shown in this section are obtained with Fourier series input. Figure 4.6 shows the PSD spectra for both the shear force (left) and the overturning moment (right). The shear force spectra are generally in good agreement, while SWASH under estimates the energy distribution of the overturning moment for the main frequency band between ~ 0.4 – 1.1 Hz.

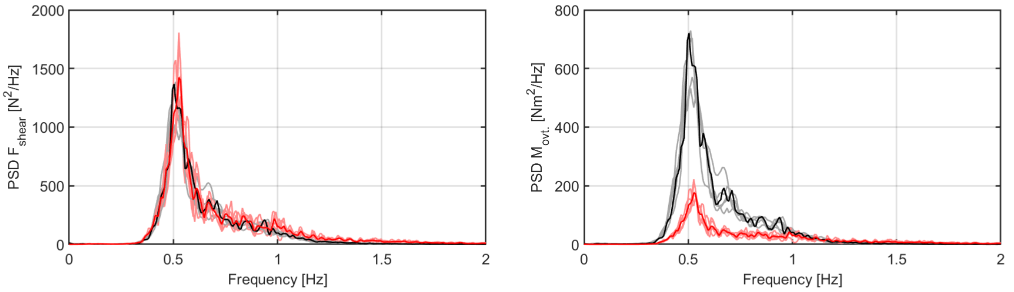

Figure 4.6: Power Spectrum Density plots of the total shear force and overturning moment for ensemble averaged nonlinear simulations (red) and experimental datasets (black).

When a short subset of the hydrodynamic loads time series is inspected, Figure 4.7, the under prediction of the overturning moment is also observed. Since the lower force transducer in the experiments is positioned below the seabed to avoid interference from the bulky sensor with the waves, there is a discrepancy between the moment reference point in the measurements and the numerical results. A post processing work around is to increase the height over which the force is distributed and correcting the moment reference point. When the total height is increased, by increasing the reference depth d_{ref}, the

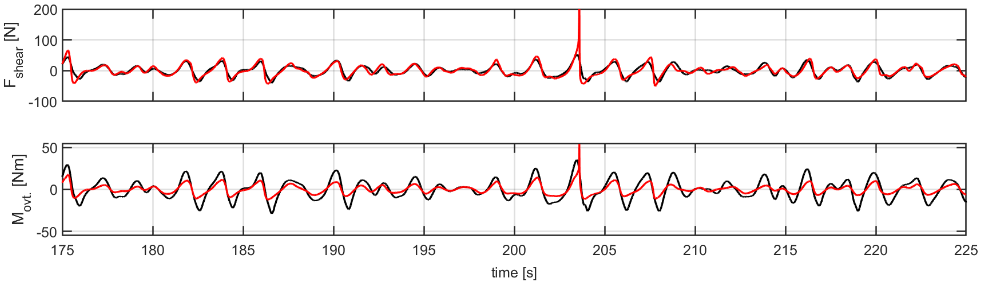

Figure 4.7: Random subset of the shear force and overturning time series from nonlinear (red) and experimental (black) with the wave maker located at wave gauge sensor 10.

overturning moment increases. The time series result can be seen in Figure 4.8.

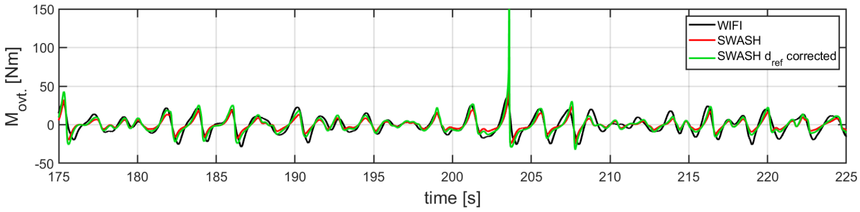

Figure 4.8: The same subset of the overturning moment time series as Figure 4.7 with a downward moment reference point correction of 0.15 m (green).

Furthermore, the time series subset in Figure 4.7 is of particular interest due to the large overshoot in the prediction of both the shear force and overturning moment. Several overshoots were observed, approximately one per full simulation. The highlighted overshoot is a result of a high and steep wave that can be seen in Figure 4.5. The steep wave front results in high particle velocities and high velocity gradients. The particle accelerations are therefore also very high, resulting in a very high shear force estimation, as the hydrodynamic force is inertia dominated. Figure 4.9 shows the fluid particle velocity and acceleration for the particular event obtained with SWASH. The measured free-surface elevation is also included in black.

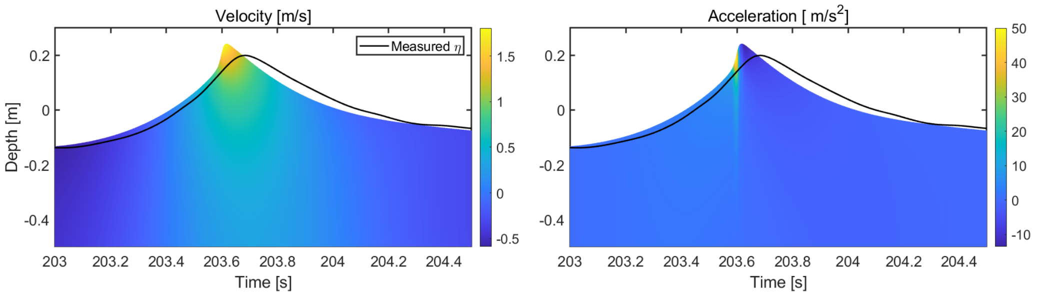

Figure 4.9: The fluid particle velocity (left) and acceleration (right) vertical distribution for SWASH over time, including the measured free-surface elevation (black). The colour map indicates the magnitude.

The velocity (left side) at the wave crest is significantly higher compared to other wave crests in the time series. The peak velocity combined with the steep wave front, indicates the potential for wave breaking. The measurements, however, show a smoother wave crest, indicating that the actual energy dissipation during the breaking process is greater than what the model captures. As discussed in subsection 2.4.3, SWASH resolves wave breaking by enforcing momentum conservation across the discontinuity at the wave front. While this approach captures the bulk characteristics of the wave dynamics, it does not fully account for the complex turbulence and energy dissipation associated with real wave breaking, leading to an underestimation of energy loss and consequently higher local velocities.

Attempts to improve the model's accuracy by including a $k-\epsilon$ turbulence model did not reduce the overshoot, as demonstrated in Figure 4.10.

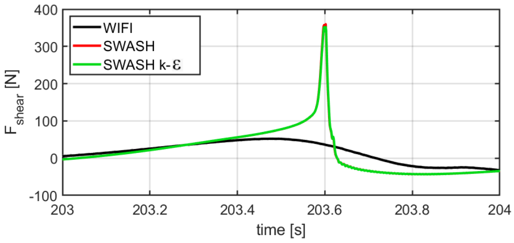

Figure 4.10: An outlier in the total shear force time series from a SWASH simulation with and without k-ϵ turbulence model included, compared with the measurement data.

5

Model performance evaluation

In this chapter, the results of the hydrodynamic load predictions for offshore wind turbine support structures during storm conditions in the North Sea are presented. SWASH, a nonlinear non-hydrostatic wave model, is used in combination with the Morison equation to estimate the hydrodynamic forces acting on the structure. Key differences between the nonlinear and a linear model, commonly used in industry, are explored. The aim is to assess the accuracy and reliability of the nonlinear approach in predicting free-surface elevation, wave kinematics, and associated hydrodynamic forces.

First, free-surface and hydrodynamic force estimations for the entire sea state are evaluated. Frequency domain and statistical analyses will provide an overall assessment of the nonlinear model's behavior. The linear model results will also be included to serve as a benchmark. Five experimental datasets were used, and wave gauge measurements served as inputs for both the linear and nonlinear model. Thus, five simulations of approximately 30 minutes on model scale per model were conducted, from which ensemble averages were obtained. Since irregular waves are inherently stochastic, conducting multiple realizations of the same sea state allows for more robust and statistically significant results.

Extreme events were identified, with the four most significant ones being analyzed. Time series data for these events will be presented, followed by an assessment of the accuracy of the ultimate load estimation. Next, a final comparison will be conducted using a setup that more closely resembles the actual process of estimating the hydrodynamic loads during the design phase. Bulk wave parameters, along with a predefined spectrum shape, will be used to generate waves for both models. The results of five wave realisations of 10 minutes are presented.

5.1. Fourier series input

5.1.1. Free-surface elevation

In the frequency domain, the energy distribution is analyzed using a PSD plot and the statistical properties of the signal peaks are assessed through a probability exceedance plot. Figure 5.1 shows the PSD free-surface elevation results (left) for the experimental data, SWASH and the linear model. The bright colors depict the ensemble averaged spectra and the muted colors correspond to the individual realisations. The good agreement indicates that the wave energy distribution is captured well in both models. However, minor deviations in the spectra peaks can be observed. SWASH under predicts the magnitude of the peak by ~ 18 %. This is also reflected in Table 5.2, where the significant wave height H_{m0} for SWASH is lower, 0.21 m compared to the 0.23 from the experimental data. Both the area under the PSD and the spectral significant wave height are proportional to the total energy. On the right side of Figure 5.1, the probability exceedance results of the normalised wave heights H/H_{m0} provide a statistical comparison of the experimental data and models with good agreement of both models with the measurements. The time domain results of the free-surface elevation are shown in the bottom plot of Figure 5.4 by means of a random subset of one of the simulations. Minor deviations between the nonlinear and measured signal can be identified, especially for large waves.

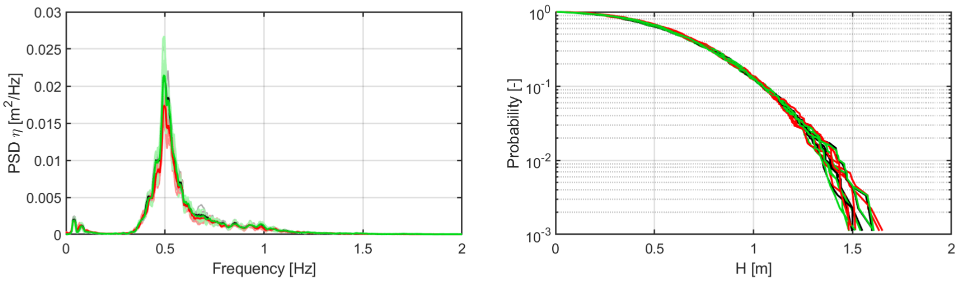

Figure 5.1: Power Spectrum Density of the free-surface elevation (left), ensemble averaged, and probability exceedance of the normalized wave heights H/H_{m0} (right) at the monopile for nonlinear model simulations (red) and the linear model (green) with Fourier input and experimental datasets (black).

5.1.2. Hydrodynamic loads

The energy distribution of the shear forces is shown in the top-left plot of Figure 5.3. The nonlinear model matches reasonably well with the experimental data, while the linear model over predicts the energy at the peak frequency by 26 %. The significant force peaks, which represent the total energy in the force signals, can be calculated similarly to significant wave height using Equation 2.12. As shown in Table 5.2, both models overestimates the significant force peak and thus the total energy.

Figure 5.3 (top right), visualises the likelihood that a certain normalised force peak F_{peak}/F_{m0} is exceeded. Both the nonlinear model and the linear model predict higher probabilities for equal peak forces compared to the experimental results. For the largest peaks in the tail of the probability exceedance, the linear model tends to align better with the experiments, while the nonlinear model predicts significantly higher force peaks, reaching over 8 times the significant force for one realization. The overshoots were already observed and briefly explored during validation in section 4.2. The kinematics of one of these overshoots is shown in Figure 5.2. SWASH kinematics are shown in the top and linear kinematics below. Where the particle velocities are similar, the particle accelerations for SWASH are three times larger (~60 m $/s^2$) than the linear accelerations (~20 m $/s^2$). The slope of the wave front for SWASH is also much steeper than the experimental data.

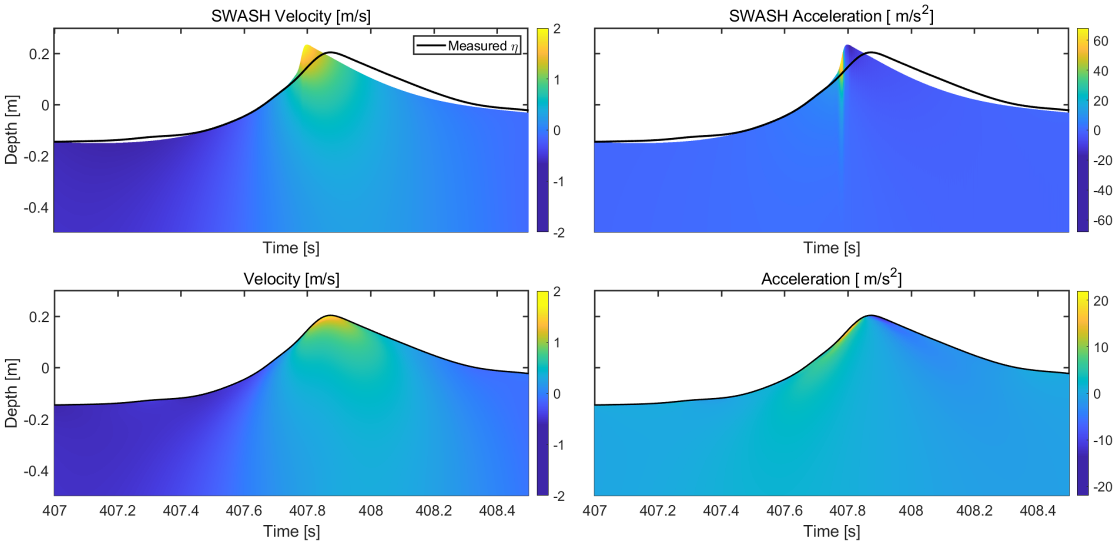

Figure 5.2: The fluid particle velocity (left) and acceleration (right) vertical distribution of an overshoot observed in SWASH (top) and the same wave event from linear wave theory (bottom), including the measured free-surface elevation (black). The colour map indicates the magnitude.

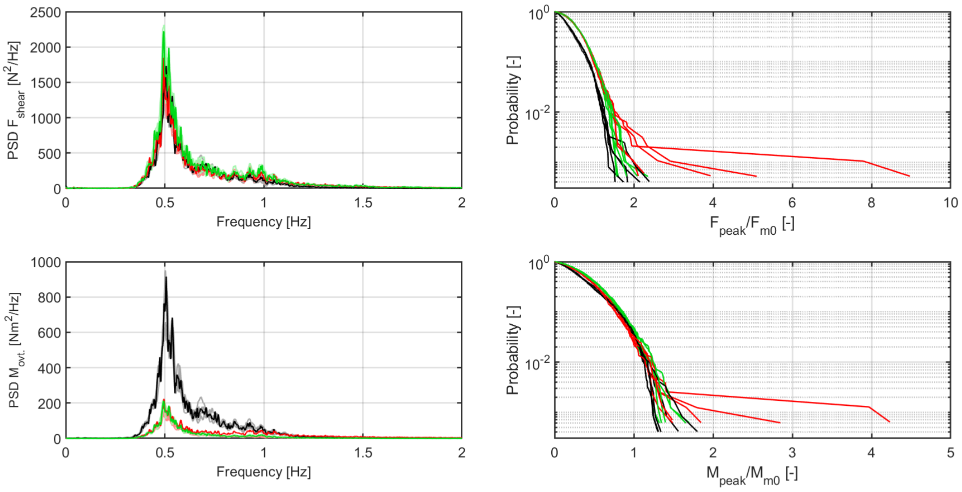

Figure 5.3: Power Spectrum Density (left) of the shear force (top) and overturning moment peaks (bottom), ensemble averaged, and probability exceedance (right) of the normalized force F/F_{m0} and moment M/M_{m0} for nonlinear model simulations (red), linear model (green) with Fourier input and experimental datasets (black).

The nonlinear model, and to a slightly lesser extent the linear model, underestimate the energy of the overturning moment in the main frequency range of approximately 0.4 to 1 Hz, as shown in Figure 5.3 (bottom-left). A significant mismatch in energy distribution is observed between the model predictions and the experimental results, indicating differences in how the models capture the overturning moment. Similar discrepancies were identified during the validation process described in section 4.2 and also a workaround solution is proposed.

However, the normalized load peaks M_{peak}/M_{m0} are overestimated by both the nonlinear and linear model, section 4.2 (bottom right). While the absolute estimated moments do not agree with the measurements, normalised moment peaks still allow to compare the exceedance probability, as the measurements and model results are scaled by the total energy content present in the signal. Similar to the probability exceedance of the force peaks, the nonlinear model exhibits extreme overshoots in the moment peaks. This contrast, underestimating the total energy but overestimating the exceedance probability of the peaks, suggests that both models, are more sensitive to rare, extreme events, resulting in higher peak force and moment predictions.

Moving towards the time domain analysis, a random subset of one of the datasets is shown in Figure 5.4 to evaluate the transient behaviour of the models. For non extreme wave events, small differences can be observed between the nonlinear model and experimental data. Close inspection of the extreme event around 1222 s, show some discrepancies. Both models, particularly the nonlinear model, under predict the force and moment peak. The free-surface elevation during the extreme event maintains a closer match to the experimental data. This highlights a potential decoupling between the ability of the models to capture wave kinematics and the translation of those kinematics into load predictions. This extreme event, along with three other events, will be further analysed in subsection 5.1.3.

5.1.3. Extreme events

The focus will now shift to the extreme events, in terms of high force and moment peaks, that were observed in the datasets and simulations. These events will be evaluated in time domain as the transient effects are important. The assumption is made that these force and moment peaks were caused by breaking waves causing impact loading on the monopile. Although an impact like behaviour, a steep rise to an extreme force or moment peak over a short duration, is observed in the time series, it cannot be confirmed that it is an actual breaking wave event. No visual confirmation is available for the experimental data and the identification method only captures events based on significant force peaks in a

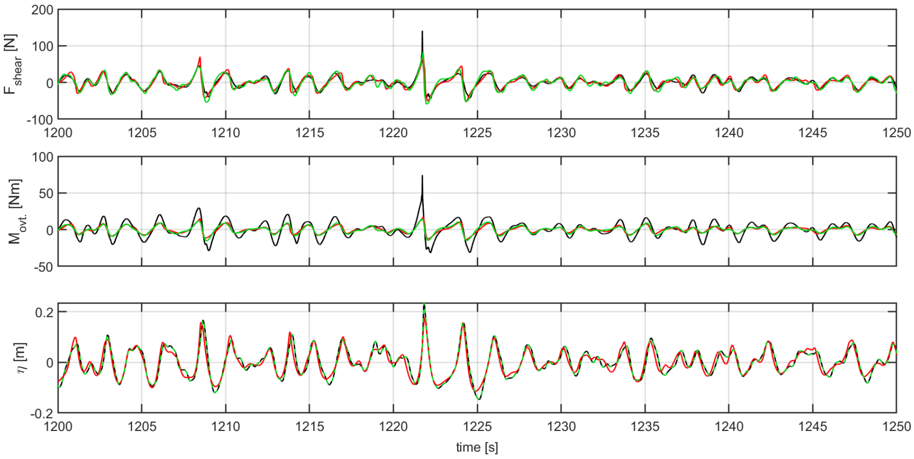

Figure 5.4: Random time series subset of the shear force, overturning moment and free-surface elevation time series from the experimental data (black), nonlinear model (red) and linear theory (dashed green) with Fourier series input.

short time frame.

The extreme events were identified with the method from Paulsen et al. [7] from subsection 2.5.3. Figure 5.5 provides an overview of the five wave realisations with extreme events indicated with a red dot. Of those extreme events, the four largest events are extracted for further analysis, indicated by green markers in Figure 5.5. For these events, the linear model is extended with the slamming model described in subsection 2.5.4.

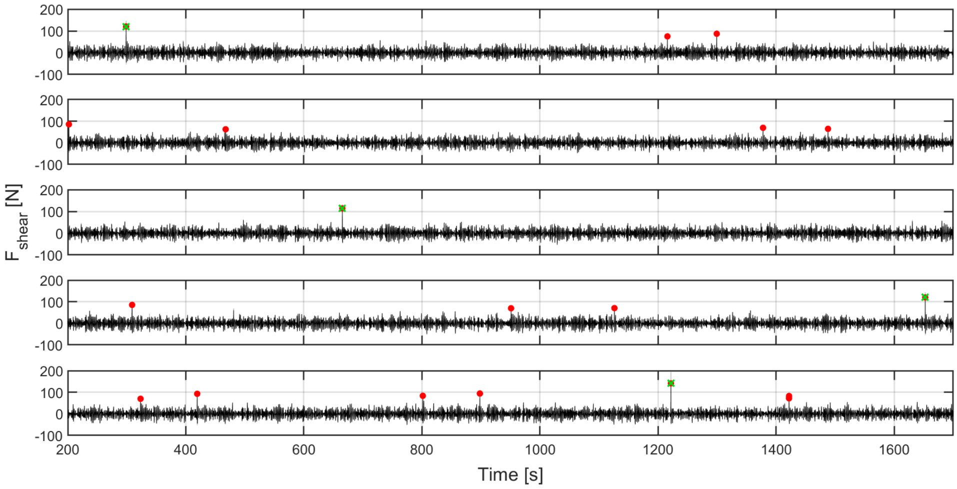

Figure 5.5: Shear force time series for the five experimental datasets with indicated extreme or slamming events (red), the four largest hydrodynamic load events are indicated with green crosses.

The four events have both the highest force and highest moments. In Figure 5.6 the time series for the shear force (top row), overturning moment (middle row) and free-surface elevation (bottom row) are shown for these events. The differences are also quantified in terms of the free-surface, force and moment characteristics and the error compared to the measurements, see Table 5.1. The nonlinear force shows large discrepancies. Where the error with the measurements ϵ_F is low for the first event, both large over estimations (event 3, $\epsilon_F \sim 88\%$) and under estimations (event 4, $\epsilon_F \sim -39\%$) can be observed. The large mismatch of the overturning moment is a known problem by now, see section 4.2.

However, when the overall shape of the time series is inspected, similar behaviour as for the shear force can be observed.

Regarding the linear model with slamming included, the shear force estimates are in better agreement with the measurements but not generally conservative. The overturning moment is largely under estimated. Even when the slamming model is included the error is > 40 %.

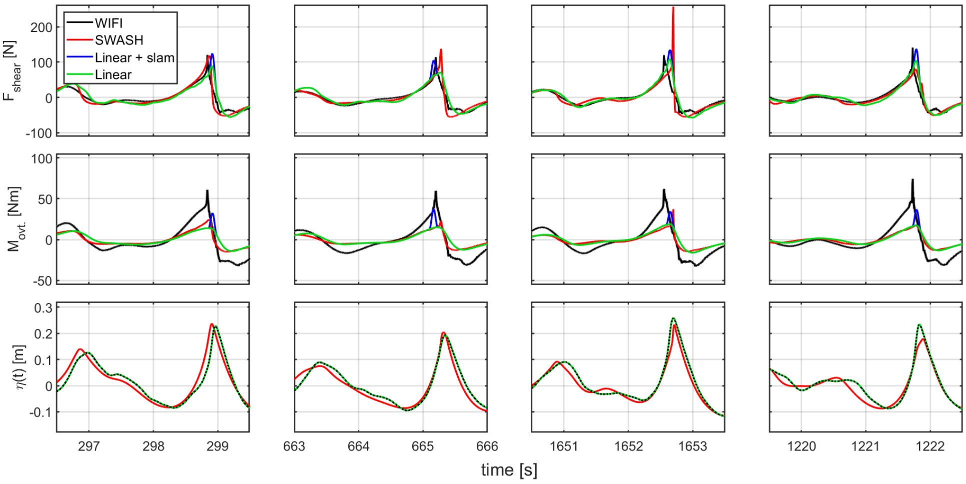

Figure 5.6: Total shear force (top row), overturning moment (middle row) and free-surface elevation (bottom row) time series for the experimental data (black), nonlinear model (red) and linear model with (blue) and without slamming model (green) for the four most extreme events.

Table 5.1: Extreme wave and hydrodynamic load characteristics and errors compared to the measurements of the four most extreme events.

		H [m]	ϵ_H [%]	T [s]	ϵ_T [%]	F_{peak} [N]	ϵ_F [%]	M_{peak} [Nm]	ϵ_M [%]
Event 1	Experiment	0.32	-	1.51	-	140.29	-	74.37	-
	Nonlinear	0.32	1.68	1.64	8.61	127.71	-8.96	28.36	-61.86
	Linear	0.32	0.19	1.51	0.03	110.29	-21.39	20.10	-72.98
	Linear + slam	-	-	-	-	145.98	4.05	38.61	-48.08
Event 2	Experiment	0.29	-	1.70	-	137.09	-	76.40	-
	Nonlinear	0.30	4.48	1.76	3.53	146.09	6.57	26.75	-64.99
	Linear	0.29	0.10	1.70	0.01	91.86	-32.99	21.00	-72.51
	Linear + slam	-	-	-	-	125.96	-8.11	43.22	-43.42
Event 3	Experiment	0.31	-	1. 75	-	143.76	-	79.11	-
	Nonlinear	0.30	-7.11	1.77	1.14	269.85	87.72	41.52	-47.52
	Linear	0.31	-0.35	1.75	0.12	136.65	-4.95	25.87	-67.29
	Linear + slam	-	-	-	-	162.42	12.98	41.23	-47.88
Event 4	Experimental	0.32	-	1.28	-	155.60	-	85.20	-
	Nonlinear	0.27	-17.82	1.46	14.06	95.42	-38.68	22.49	-73.60
	Linear	0.32	0.15	1.28	-0.06	126.56	-18.66	23.26	-72.70
	Linear + slam	-	-	-	-	159.27	2.36	42.67	-49.91

5.2. Bulk wave parameter input

To evaluate how the results differ when using bulk wave parameters instead of Fourier series from measurements, new simulations were performed with both the nonlinear and linear model using the alternative input method. Furthermore, the wave maker is placed much further away from the target location. The results from SWASH are directly extracted from that location and the linear results are phase shifted so that the time series will correspond to the same location. The overturning moment is not included in the analysis, the overall trend is comparable to the results of previous chapters; significant difference with the measurements was observed.

The PSD results can be seen on the left side of Figure 5.7 and 5.8. The nonlinear model under predicts the total energy for The free-surface elevation η which is also reflected in Table 5.2. The shear force F_{shear} energy distribution over the frequencies and total energy is in good agreement.

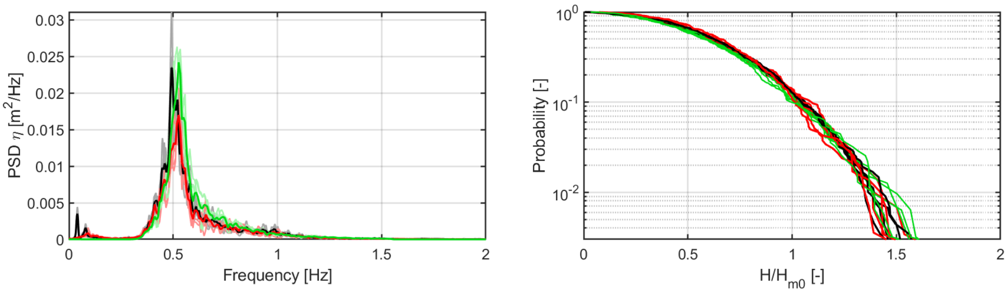

Figure 5.7: Power Spectrum Density of the free-surface elevation (left), ensemble averaged, and probability exceedance of the normalized wave heights H/H_{m0} (right) at the monopile for nonlinear simulations (red) and the linear model (green) with bulk wave parameter input compared with experimental data (black).

The nonlinear model shows higher probabilities for the normalised force and moment peaks compared to the measured data and the tail of the normalised force peak F_{peak}/F_{m0} exceedance probability highlights the sensitivity to the extreme events, resulting in higher peak force and moment predictions. The highest force peaks per event are 3.5 - 6.5 times higher than the significant force peak. The linear model is conservative in terms of exceedance probability for the less extreme events but underestimate the most extreme force peaks.

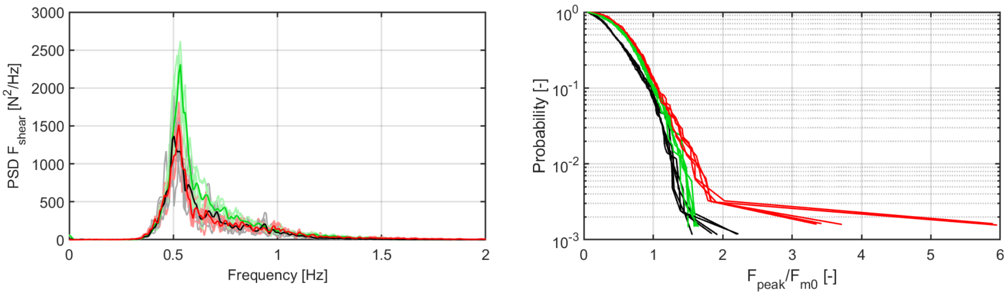

Figure 5.8: Power Spectrum Density (left) of the shear force, ensemble averaged, and probability exceedance (right) of the normalized force F/F_{m0} for nonlinear simulations (red) and linear model (green) with bulk wave parameter input compared with experimental data (black).

Time series analysis does not yield significant insights as a deterministic comparison is not possible due to the random distribution of phase angles. To still provide some insights into extreme events, the ten highest force peaks from the measured datasets, as well as from the nonlinear and linear simulations, are obtained and compared in Table 5.3. The extreme peak forces demonstrate that the nonlinear model significantly over predicts the most extreme force peaks, with a wide range of estimates indicating considerable variability in the predictions. It is important to account for the total simulation time

Table 5.2: Ensemble averaged significant wave height, shear force and overturning moment peak and their mean periods for SWASH and linear model with bulk wave parameter input.

	H_{m0} [m]	F_{m0} [N]	M_{m0} [Nm]
Experiment	0.225	62.32	44.07
Nonlinear Fourier	0.208	66.73	19.57
Linear Fourier	0.224	73.06	20.89
Nonlinear spectrum	0.207	65.62	-
Linear spectrum	0.231	77.05	-

when comparing these results. The experimental data used to extract the extreme events span approximately 120 minutes after accounting for spin-up and spin-down, while the simulations only provide around 40 minutes of steady-state data. The longer duration of the experimental data increases the likelihood of capturing rare and extreme events, resulting in higher observed force peaks. Extending the numerical simulations to 120 minutes would likely lead to even higher predicted nonlinear (and linear) force peaks. Thus, the difference in duration can skew the comparison, potentially causing the shorter simulations to underestimate the frequency and magnitude of extreme events.

The linear model shows more consistent estimates but remains non-conservative for the most extreme events, as the range of extreme force peak estimates is much narrower compared to the measurements. It is also important to note that the linear model was not extended with a slamming model, as it was not possible to identify slamming events using the identification method of Paulsen et al. [7] (subsection 2.5.3). The relationship between wave height and force peak is most evident for the linear model, where a clearer correlation is observed. In contrast, the nonlinear model predicts higher peak forces even for waves with similar heights, resulting in a wider range of force estimates.

Table 5.3: Ten highest force peaks with accompanying wave heights of 5 datasets of the measurements and the highest force peaks of the 5 simulations nonlinear and linear model).

	Experiment		Nonlinear		Linear	
Event	F_{peak} [N]	H [m]	F_{peak} [N]	H [m]	F_{peak} [N]	H [m]
1	155.60	0.32	394.73	0.27	127.90	0.39
2	143.76	0.31	381.50	0.34	125.85	0.36
3	140.29	0.32	245.46	0.32	124.79	0.37
4	137.09	0.29	223.92	0.26	122.95	0.36
5	134.24	0.35	217.57	0.33	122.58	0.36
6	119.37	0.33	131.18	0.32	120.72	0.37
7	116.81	0.34	126.55	0.33	120.45	0.37
8	116.02	0.33	121.29	0.30	117.60	0.36
9	114.48	0.32	117.14	0.31	116.54	0.35
10	101.87	0.40	115.42	0.27	116.12	0.33

6

Discussion

The well-known quote from the famous statistician George Box: "All models are wrong, but some are useful.", reminds us that while models may never perfectly capture the full complexity of natural systems, they are essential tools for approximating and understanding real-world phenomena. The objective of this research project has been to evaluate such a tool, a nonlinear model to obtain hydrodynamic load estimations on offshore wind turbine support structures for the design phase. Fully nonlinear wave kinematics are obtained with the non-hydrostatic model SWASH and the loads are calculated using the Morison equation. The focus of this study has been on storm wave conditions, with particular attention given to extreme events, where nonlinear effects and transient behaviour are most pronounced.

This chapter will delve into the implications of the results. First the interpretation of the results from chapter 4 and chapter 5 will be discussed in section 6.1. Limitations as well and explanations will be given for discrepancies. Finally, section 6.2 will suggest directions for future research, addressing the limitations encountered in this project.

6.1. Interpretation of key findings

6.1.1. Free-surface elevation

In general SWASH underestimated the total energy in the wave spectrum. The significant wave height H_{m0} at the target location for SWASH was 0.211 m for both Fourier series input and 0.207 for the bulk wave parameter input, while the measured H_{m0} is 0.225 m. The power spectrum density plots in Figure 5.1 (left) and 5.7 (left) also highlight lower energy content, especially at the peak frequency. The ensemble averaged energy at the peak is ~ 18 % lower for Fourier input compared to the lab data.

The wave maker had to be placed in close proximity (at half a peak wavelength distance ~ $0.5\lambda_p$) to achieve a deterministic comparison with the measured time series. The lack of sufficient propagation distance can result in lower energy at the peak. In contrast, for the bulk wave parameter input, the wave maker was positioned further away (~ $10\lambda_p$), allowing more space for wave propagation. However, a larger difference for in peak energy is observed, ~ 27 % lower compared to the experimental data. This can be partially attributed to the generation of spurious waves. In SWASH, the linear boundary conditions used for wave generation produce spurious waves that are not bound to the primary wave but behave like free waves. These spurious waves can interfere destructively with the target wave conditions, resulting in lower energy redistribution in the simulation, as discussed in subsection 2.4.2. Extending the inflow boundary condition to second order can help reduce these spurious waves and their impact on the free-surface elevation, potentially improving the energy distribution in the PSD plot. When Fourier series are used as input into SWASH, the model does not need to explicitly generate the bound waves, as the nonlinear phase coupling is already included in the wave spectrum. Phase coupling results in less significant spurious waves while nonlinearity is preserved to some extent.

The probability distribution of wave heights, shown as the probability of exceedance of normalized wave heights (H/H_{m0}) in Figure 5.1, indicates that SWASH accurately captures the range of individual wave heights, including those associated with breaking waves. Despite using a simplified approach to handle breaking waves, the model still represents the bulk wave characteristics well. This suggests that the nonlinear effects incorporated through phase coupling help maintain realistic wave dynamics.

Since the Fourier series for the linear wave model are obtained from the monopile location, an good match of the free-surface elevation is expected as wave components up to 10 Hz are included. The energy distribution, total energy, wave height probability exceedance and time series closely align with the experimental data. When the bulk wave parameters are used, larger discrepancies are observed. The significant wave height is slightly over predicted at 0.231 m.

6.1.2. Hydrodynamic loads

The wave elevation provides an indication of the wave model performance, but it is the wave kinematics that ultimately determine the hydrodynamic loads. Since the wave kinematics were not measured, they cannot be directly validated. Therefore, any discrepancies in the forces between the models and experimental data may result either from inaccuracies in the modelled kinematics or from errors in translating the kinematics into hydrodynamic loads. As shown in the force and moment PSD spectra from Figure 5.3 and 5.8 (left), the energy distribution of the nonlinear shear shear force closely aligned with the experimental data but the significant force peaks are slightly over estimated (~ 7%), see Table 5.2.

However, the individual force peaks F_{peak}, normalized with the significant force peak F_{m0}, do not match, especially the extreme events with low probabilities, Figure 5.3 and 5.8 (right). These extreme force peaks are present in both the Fourier input results and the bulk wave parameter input. The highest F_{peak} values from the measured data are in the range of $1.5 - 2.3$ times F_{m0}. In Figure 5.3 (right) 7 events can be identified with F_{peak}/F_{m0} values larger than 2.3 across 3 simulations. For the bulk wave parameter input, (Figure 5.8 right) 5 events, 1 per simulation, are observed. Thus, the Fourier series input shows large variability of the number of overshoots per simulation.

Time domain analysis of the nonlinear shear force further highlights these extreme overshoots, which are explored in section 4.2. The high forces correspond to very high particle accelerations, reaching up to 50 $\mathrm{m/s^2}$ for a particular event (see Figure 4.9). The particle acceleration is calculated during post-processing by taking the gradient of the velocity, which may introduce errors if the velocity field is overestimated.

The overshoots in SWASH can be attributed to the absence of wave generated turbulence, which leads to an overestimation of local particle velocity. Figure 4.9 and 5.2 show that the velocity at the wave crest is significantly higher than surrounding particle velocities, and the wave front is very steep, suggesting the wave is likely breaking. However, since SWASH is a single-valued free-surface model, it cannot simulate the wave overturning process. In reality, a plunging breaker would generate a turbulent water-air mixture that results in damping and dissipation of energy through heat and noise. The absence of wave breaking turbulence in SWASH results in an overestimation of wave kinematics, leading to exaggerated hydrodynamic loads. Measurements of the wave kinematics are not available, so a comparison with actual kinematics is not possible. However, the free-surface for the experimental data (black line in Figure 4.9) shows a much smoother wave crest, indicating that the actual energy dissipation is greater than what is simulated in SWASH. Furthermore, in Figure 5.2 (bottom) also the linear kinematics for the same wave event can be seen. Where the particle velocities are similar for both SWASH and linear, the peak acceleration for SWASH is approximately three times larger compared to linear. The velocity gradient are thus much higher. The wave front slope from the experimental data is again much smoother opposed to the very steep wave front in the SWASH results. The $k-\epsilon$ turbulence model did not reduce the overshoot (Figure 4.10) because it may not effectively dissipate the energy at the scale needed during wave breaking in SWASH. The $k-\epsilon$ model is designed for steady-state turbulence and equilibrium conditions, making it suitable for fully developed turbulent flows, which is not the case here where rapid, non-equilibrium turbulence occurs during wave breaking.

The nonlinear significant overturning moment peak, which is proportional to the total energy, is under-predicted by approximately 55 %. This discrepancy in overturning moment predictions has been consistently observed across all analyses. One possible explanation is a mismatch in the vertical reference point used for the calculations. While applying a correction to the reference point, as described in section 4.2, improves the results, the correction is arbitrary and has not been pursued further. Nevertheless, normalizing the moment peaks with the significant moment M_{m0} (Figure 5.3, bottom right) still offers some insights. Similar overshoots are observed as for the shear force peaks further indicating that SWASH overestimates the wave kinematics, leading to higher predicted forces.

The time series subset of the hydrodynamic loads for the Fourier series input (Figure 5.4) allow for a qualitative analysis. Visual observation of this random subset indicates general agreement of the models with the experimental data. However, extreme events or force peaks show discrepancies and these will be discussed in the next section.

6.1.3. Extreme events

While the previous sections analysed the overall behaviour of the nonlinear model, this section focuses specifically on the most extreme events. Figure 5.6 displays the four most extreme events from the five measurement datasets used in this project, with accompanying wave and load characteristics presented in Table 5.1. The wave height errors ϵ_H range from approximately -7 - 18 %. However, much larger discrepancies are observed in the hydrodynamic load predictions. The nonlinear model exhibits significant over estimations (e.g., event 3, with ϵ_F around 88 %) and under estimations (event 4, ϵ_F around -39 %). These inconsistencies suggest that the nonlinear force estimates are neither consistently conservative nor reliably accurate across different extreme events.

The large overestimation for event 3 can be attributed to the very steep wave front, similar to the overshoot previously explored in section 4.2. The steepness of the wave front leads to high local particle accelerations and velocities, which are not adequately damped due to the lack of breaking wave turbulence modelling. This results in exaggerated force predictions. The under prediction of the hydrodynamic load in event 4 is possibly related to the lower wave height and slope of the wave front for SWASH, shown in the bottom right of Figure 5.6. The lower wave slope suggests that the wave crest is not as sharp or pronounced in SWASH, which could be due to the close proximity of the wave maker to the target location. The short propagation distance limits the development of nonlinear effects in the free-surface elevation, resulting in underdeveloped wave steepness and thus under estimated wave kinematics, resulting in less intense hydrodynamic loads for this event.

The linear model is extended with the slamming model, discussed in subsection 2.5.4. The slamming model significantly improved the force estimates. The linear model was generally non conservative, most significantly for event 2 with an under prediction of around 33 %. The slamming model improved the force peak error to approximately -8 % and made the other events slightly conservative, over estimating the force peak by 2-13 %. The linear model outperforms the nonlinear model significantly for the extreme events.

For the bulk wave parameter input, a statistical comparison can be made with the experimental data. Table 5.3 shows the ten most extreme events in terms of shear force peak. The nonlinear force peaks are significantly higher, especially the first five events. The maximum force peak for the experimental data is 156 N. The five highest events in the nonlinear simulations range between 217 - 395 N which is 40 - 154 % higher than the highest measured force peak. The nonlinear model is thus extremely conservative for the most extreme events. These extremely conservative estimates are a result from high wave kinematics due to a lack of wave generated turbulence in SWASH. Longer duration simulations have a higher probability of including rare and extreme events. The 120 minute experimental dataset naturally captures more extreme events than the 40 minute simulations due to its extended duration. Therefore, the shorter simulation duration may result in an underestimation of the true range of extreme forces, further emphasizing the conservative nature of the nonlinear models. In contrast, the linear model is non conservative for the five largest force peaks. However, it does not incorporate an embedded extreme design wave or a slamming model, making it insufficient for providing conservative force estimates for extreme events. This underscores the importance of including nonlinear wave dynamics, as linear wave kinematics alone are inadequate for capturing the full extent of extreme forces. Given the shorter 40 minute simulation duration, the linear model's extreme values might also be underestimated compared to the experiments.

6.2. Future studies

One key area for future research is the exploration of turbulence modelling to improve wave breaking representation in SWASH. The overestimation of wave kinematics observed in this study, which led to large force peak overshoots, underscores the need for better capturing of local energy dissipation due to wave breaking. Incorporating such modelling could help account for energy dissipation during breaking, reducing the exaggerated wave kinematics and enhancing the accuracy of hydrodynamic load predictions.

In subsection 2.4.2 it was mentioned that second order wave generation is possible but only for a vertical resolution up to 4 layers. For conditions where wave breaking can occur, SWASH requires a much higher vertical resolution to capture the sharp changes in free-surface elevation and velocity during a breaking wave event. Improving the wave generation to second order for higher vertical resolution would decrease the effects of spurious waves.

The linear model was used primarily as a benchmark for evaluating the nonlinear model, with a basic implementation. To better align with industry practices, the linear wave model could be enhanced by incorporating an embedded extreme design wave, which would improve its representation of extreme events when bulk wave parameter input is used. Linear wave theory cannot capture the nonlinear characteristics of steep waves, but an embedded extreme wave can approximate the conditions of an extreme event. Additionally, incorporating a slamming model could provide a more accurate and conservative estimate of hydrodynamic loads.

Conducting a new set of physical experiments is recommended to address multiple issues simultaneously. New experiments can resolve the lack of documentation regarding, for example the measurement methodology for the wave-induced moments. Additionally, coupling these experiments with numerical simulations would allow for deterministic comparisons in the time domain. By storing the amplitude and phase of each wave component used to generate the input signal for the physical wave maker, the same conditions can be replicated in SWASH, facilitating phase synchronization and direct comparison. When the wave maker can be placed sufficiently far from the target location, the nonlinear wave evolution can be validated. Preferably the wave kinematics, e.g. the particle velocities, are measured so that they can be validated as well. Accurate validation of these kinematics is essential for identifying the source of discrepancies observed during extreme events. With validated kinematics, it will be clearer whether the inaccuracies in hydrodynamic load predictions arise from the kinematic representation itself or from the transformation of these kinematics into forces using the Morison equation.

7

Conclusion

This research aimed to evaluate the performance of the non-hydrostatic SWASH model in simulating fully nonlinear wave kinematics and estimating hydrodynamic loads, using the Morison equation, on offshore wind turbine support structures under storm conditions. The nonlinear model was compared to experimental data to validate and evaluate its performance, with a linear model serving as a benchmark for the industry standard.

For deterministic comparison with available experimental datasets, Fourier series obtained from measured free-surface elevation signal, were used for generating waves in SWASH. The free-surface elevation was accurately represented in terms of statistical distribution of wave heights but underestimated the energy at the peak frequency and the spectral significant wave height. The differences can be attributed to the close proximity of the wave maker, which was required to achieve phase synchronization. The energy distribution of the shear force was well captured by the nonlinear model but the force peaks, obtained with a zero-crossing analysis showed discrepancies. Several overshoots were observed in terms of hydrodynamic loading which can be attributed to the lack of wave breaking turbulence modelling in SWASH. For the extreme events that were identified in the experimental datasets, the nonlinear model estimates were of mixed accuracy. Both a significant over estimation and under estimation were observed. The over estimation can be attributed to exaggerated particle acceleration from SWASH, similar to the overshoots for non extreme events. The under estimation can be attributed to a lower wave height and slope of the wave front, resulting in underestimated wave kinematics. The linear model, extended with a slamming model, showed much better performance in terms of shear force peak estimation. The overturning moment estimates were consistently lower than the measured values. One possible explanation is that the reference point for the measured moment may have been positioned below the actual seafloor, though this remains uncertain. As a result, the analysis of the overturning moment should be interpreted with caution, and its its value may be limited.

While the Fourier series allowed for deterministic comparison, free-surface elevation measurements are not available during the design phase of an offshore wind turbine. Bulk wave parameter input, used to obtain a random wave spectrum represents the industry method of obtaining wave realisations. The statistical distribution of the wave heights was accurately represented by both SWASH and the linear wave model. Discrepancies were observed when the hydrodynamic loads were calculated with the Morison equation. For the nonlinear model, again large overshoots were observed. The linear model estimated non conservative extreme force peaks. However, the linear wave model was not extended with an extreme design wave and the slamming could also not be applied.

In conclusion, the research objective to evaluate the performance of SWASH combined with the Morison equation for estimating hydrodynamic loads under storm conditions indicates that the performance is limited. Significant overshoots were observed for non-extreme events, and the results for extreme events were inconsistent, highlighting challenges in accurately capturing the hydrodynamic loads. This variability suggests that while SWASH offers valuable insights into nonlinear wave behaviour, further refinement is necessary before it can be fully relied upon for accurate load estimations in offshore wind turbine design.

The implementation of SWASH was limited due to the requirement of the close proximity of the wave maker to the target location for the deterministic analysis and the linear inflow boundary condition, resulting in generation of spurious waves that possibly interfered with the wave field. Future studies should mainly focus on improving the wave kinematics for SWASH by extending the inflow boundary conditions to second order wave generation and exploring turbulence modelling.

Bibliography

[1] Global Wind Energy Council, "Global wind report 2024," Global Wind Energy Council, 2024, Accessed: 2024-10-10. [Online]. Available: `https://gwec.net/wp-content/uploads/2024/05/GWR-2024_digital-version_final-2.pdf`.

[2] S. Rodrigues, C. Restrepo, G. Katsouris, et al., "A multi-objective optimization framework for offshore wind farm layouts and electric infrastructures," Energies, vol. 9, no. 3, p. 216, 2016.

[3] L. H. Holthuijsen, Waves in Oceanic and Coastal Waters. Cambridge: Cambridge University Press, 2007, ISBN: 9780521860284.

[4] B. Le Méhauté, An introduction to hydrodynamics and water waves. Springer Science & Business Media, 1976.

[5] S. K. Chakrabarti, Hydrodynamics of offshore structures. WIT press, 1987.

[6] J. Wienke and H. Oumeraci, "Breaking wave impact force on a vertical and inclined slender pile — theoretical and large-scale model investigations," Coastal Engineering, vol. 52, no. 5, pp. 435–462, 2005, ISSN: 0378-3839. DOI: `https://doi.org/10.1016/j.coastaleng.2004.12.008`. [Online]. Available: `https://www.sciencedirect.com/science/article/pii/S0378383904001735`.

[7] B. T. Paulsen, B. de Sonneville, M. van der Meulen, and N. G. Jacobsen, "Probability of wave slamming and the magnitude of slamming loads on offshore wind turbine foundations," Coastal Engineering, vol. 143, pp. 76–95, 2019, ISSN: 0378-3839. DOI: `https://doi.org/10.1016/j.coastaleng.2018.10.002`. [Online]. Available: `https://www.sciencedirect.com/science/article/pii/S0378383917301928`.

[8] IEA, World energy outlook 2023, IEA, Paris, 2023. [Online]. Available: `https://www.iea.org/reports/world-energy-outlook-2023`.

[9] O. Edenhofer, R. Pichs-Madruga, Y. Sokona, et al., IPCC Special Report on Renewable Energy Sources and Climate Change Mitigation. Cambridge University Press, 2011.

[10] T. Mai, R. Wiser, D. Sandor, et al., Renewable electricity futures study (executive summary), 2012. [Online]. Available: `https://www.nrel.gov/analysis/re-futures.html`.

[11] WindEurope, Wind energy in europe: 2023 statistics and the outlook for 2024-2030, WindEurope, 2024. [Online]. Available: `https://windeurope.org/intelligence-platform/product/wind-energy-in-europe-2023-statistics-and-the-outlook-for-2024-2030/`.

[12] International Energy Agency, "Offshore wind outlook 2020," International Energy Agency, 2020, Accessed: 2024-09-04. [Online]. Available: `https://www.iea.org/reports/offshore-wind-outlook-2020`.

[13] F. Zahle, A. Barlas, K. Lønbæk, et al., Definition of the IEA Wind 22-Megawatt Offshore Reference Wind Turbine, English. Technical University of Denmark, 2024, DTU Wind Energy Report E-0243 IEA Wind TCP Task 55. DOI: `10.11581/DTU.00000317`.

[14] P. Bortolotti, K. Dykes, K. Merz, L. Sethuraman, and F. Zahle, "Definition of the iea wind 10-megawatt offshore reference wind turbine," National Renewable Energy Laboratory (NREL), Tech. Rep., 2019. [Online]. Available: `https://www.nrel.gov/docs/fy19osti/73492.pdf`.

[15] E. Gaertner, J. Rinker, L. Sethuraman, et al., Definition of the iea 15-megawatt offshore reference wind turbine, 2020. [Online]. Available: `https://www.nrel.gov/docs/fy20osti/75698.pdf`.

[16] ABS, "Design standards for offshore wind farms," M10PC00105, 2011.

[17] "Wind energy generation systems - Part 3-1: Design requirements for fixed offshore wind turbines," International Electrotechnical Commission, Geneva, CH, Standard, Apr. 2019.

[18] "Environmental conditions and environmental loads," Det Norske Veritas, Standard, Sep. 2019. [Online]. Available: `https://www.dnv.com/oilgas/download/dnv-rp-c205-environmental-conditions-and-environmental-loads.html`.

[19] G. B. Airy, Tides and waves. B. Fellowes, 1845.

[20] K. O. Olafsson and O. T. Gudmestad, “A single extreme stream function wave embedded in linear random waves,” International Journal of Offshore and Polar Engineering, vol. 18, no. 3, pp. 176–182, 2008.

[21] P. S. Tromans, A. R. Anaturk, and P. Hagemeijer, “A new model for the kinematics of large ocean waves - application as a design wave,” Proceedings of the First International Offshore and Polar Engineering Conference, vol. 3, pp. 64–71, 1991.

[22] J. Morison, J. Johnson, and S. Schaaf, “The Force Exerted by Surface Waves on Piles,” Journal of Petroleum Technology, vol. 2, no. 05, pp. 149–154, May 1950, ISSN: 0149-2136. DOI: `10.2118/950149-G`.

[23] A. Ghadirian and H. Bredmose, “Pressure impulse theory for a slamming wave on a vertical circular cylinder,” Journal of Fluid Mechanics, vol. 867, R1, 2019. DOI: `10.1017/jfm.2019.151`.

[24] F. Shi, R. A. Dalrymple, J. T. Kirby, Q. Chen, and A. Kennedy, “A fully nonlinear boussinesq model in generalized curvilinear coordinates,” Coastal Engineering, vol. 42, no. 4, pp. 337–358, 2001.

[25] A. P. Engsig-Karup, H. B. Bingham, and O. Lindberg, “An efficient flexible-order model for 3d nonlinear water waves,” Journal of computational physics, vol. 228, no. 6, pp. 2100–2118, 2009.

[26] M. Zijlema, G. Stelling, and P. Smit, “Swash: An operational public domain code for simulating wave fields and rapidly varied flows in coastal waters,” Coastal Engineering, vol. 58, no. 10, pp. 992–1012, 2011.

[27] C.-L. Navier, “Mémoire sur les lois du mouvement des fluides,” Mémoires de l’Académie Royale des Sciences de l’Institut de France, vol. 6, pp. 389–440, 1823.

[28] G. G. Stokes, “On the theories of the internal friction of fluids in motion and of the equilibrium and motion of elastic solids,” Transactions of the Cambridge Philosophical Society, vol. 8, pp. 287–319, 1845.

[29] K. Hasselmann, T. P. Barnett, E. Bouws, et al., “Measurements of wind-wave growth and swell decay during the joint north sea wave project (jonswap).,” Ergaenzungsheft zur Deutschen Hydrographischen Zeitschrift, Reihe A, 1973.

[30] W. J. Pierson Jr and L. Moskowitz, “A proposed spectral form for fully developed wind seas based on the similarity theory of sa kitaigorodskii,” Journal of geophysical research, vol. 69, no. 24, pp. 5181–5190, 1964.

[31] R. G. Dean, “Stream function representation of nonlinear ocean waves,” Journal of Geophysical Research, vol. 70, no. 18, pp. 4561–4572, 1965.

[32] D. J. Korteweg and G. de Vries, “On the change of form of long waves advancing in a rectangular canal, and on a new type of long stationary waves,” Philosophical Magazine, vol. 39, no. 240, pp. 422–443, 1895. DOI: `10.1080/14786449508620739`.

[33] A. Ghadirian, F. Pierella, and H. Bredmose, “Calculation of slamming wave loads on monopiles using fully nonlinear kinematics and a pressure impulse model,” Coastal Engineering, vol. 179, p. 104 219, 2023, ISSN: 0378-3839. DOI: `https://doi.org/10.1016/j.coastaleng.2022.104219`. [Online]. Available: `https://www.sciencedirect.com/science/article/pii/S0378383922001326`.

[34] B. Robertson, K. Hall, R. Zytner, and I. Nistor, “Breaking waves: Review of characteristic relationships,” Coastal Engineering Journal, vol. 55, no. 01, p. 1 350 002, 2013.

[35] Y. Goda, “A study on impulsive breaking wave force upon a vertical pile,” Rept. Port and Harbour Res. Inst., vol. 5, no. 6, pp. 1–30, 1966.

[36] J. A. Battjes and J. Janssen, “Energy loss and set-up due to breaking of random waves,” in Coastal engineering 1978, 1978, pp. 569–587.

[37] E. B. Thornton and R. Guza, “Transformation of wave height distribution,” Journal of Geophysical Research: Oceans, vol. 88, no. C10, pp. 5925–5938, 1983.

[38] M. Zijlema, “Computation of free surface waves in coastal waters with swash on unstructured grids,” Computers & Fluids, vol. 213, p. 104 751, 2020.

[39] M. Zijlema and G. Stelling, “Efficient computation of surf zone waves using the nonlinear shallow water equations with non-hydrostatic pressure,” Coastal Engineering, vol. 55, no. 10, pp. 780–790, 2008.

[40] M. Zijlema and G. S. Stelling, “Further experiences with computing non-hydrostatic free-surface flows involving water waves,” International journal for numerical methods in fluids, vol. 48, no. 2, pp. 169–197, 2005.

[41] D. P. Rijnsdorp, P. B. Smit, and M. Zijlema, “Non-hydrostatic modelling of infragravity waves under laboratory conditions,” Coastal Engineering, vol. 85, pp. 30–42, 2014.

[42] T. Baldock and C. Swan, “Evolution of large-scale undular waves,” Journal of Fluid Mechanics, vol. 287, pp. 317–341, 1994.

[43] S. T. Grilli, J. Skourup, and I. A. Svendsen, “Numerical generation and absorption of fully nonlinear periodic waves,” Journal of Engineering Mechanics, vol. 123, no. 10, pp. 1060–1069, 1997.

[44] P. Vasarmidis, G. Klonaris, M. Zijlema, V. Stratigaki, and P. Troch, “A study of the non-linear properties and wave generation of the multi-layer non-hydrostatic wave model swash,” Ocean Engineering, vol. 302, p. 117 633, 2024.

[45] D. H. Peregrine, “Breaking waves on beaches,” in Annual Review of Fluid Mechanics, vol. 15, Annual Reviews, 1983, pp. 149–178. DOI: `10.1146/annurev.fl.15.010183.001053`.

[46] H. Lamb, Hydrodynamics, 6th. Cambridge, UK: Cambridge University Press, 1932.

[47] O. S. Madsen and I. A. Svendsen, “Turbulent bores and hydraulic jumps,” Proceedings of Coastal Engineering, vol. 1, pp. 295–308, 1983. DOI: `10.1061/9780872623736.023`.

[48] G. H. Keulegan, “Forces on sylinder and plates in an oscillating fluid,” J. Res. Nat. Bur. Stand., vol. 60, no. 5, pp. 423–440, 1958.

[49] T. Sarpkaya, Wave Forces on Offshore Structures. Cambridge: Cambridge University Press, 2010, pp. 95–98, ISBN: 9780521896252.

[50] T. Von Karman, “The impact on seaplane floats during landing,” 1929.

[51] H. Wagner, “Über stoß-und gleitvorgänge an der oberfläche von flüssigkeiten,” ZAMM-Journal of Applied Mathematics and Mechanics/Zeitschrift für Angewandte Mathematik und Mechanik, vol. 12, no. 4, pp. 193–215, 1932.

[52] I. Campbell and P. Weynberg, “Measurement of parameters affecting slamming,” Wolfson Unit for Marine Technology, Southampton, vol. 440, pp. 1–26, 1980.

[53] E. J. de Ridder, T. Bunnik, J. M. Peeringa, et al., “Summary of the joint industry project wave impact on fixed foundations (wifi jip),” in International conference on offshore mechanics and arctic engineering, American Society of Mechanical Engineers, vol. 57786, 2017, V010T09A081.

[54] SWASH, Swash user manual version 10.01a, The SWASH team, Delft Univeristy of Technology, 2024.

[55] D. H. P. C. C. (DHPC), DelftBlue Supercomputer (Phase 2), `https://www.tudelft.nl/dhpc/ark:/44463/DelftBluePhase2`, 2024.

A

Convergence study

When applying a grid based model such as SWASH, it is important to perform a convergence study. The goal of a convergence study is to find the coarsest grid that still converges to an accurate solution, as a coarser grid reduces computational resources. However, for this project, the resources of a high-performance computing cluster were available [55], making the optimization of the model setup and resolution less critical. The first test involves the setup for regular waves, where both wave height and phase angle are compared. For irregular waves, the significant wave height H_{m0} and the phase angle at the peak amplitude are evaluated. The relative error threshold is somewhat arbitrarily set to 2.5 %. However, the primary goal is not to strictly reach this threshold, but to show that the numerical errors are small enough to ensure that any discrepancies in the results later on are not caused by insufficient grid resolution.

A.1. Regular waves

The relative error of the wave height for regular waves can be seen in Figure A.1. On the left side, the relative error is shown as a function of the amount of grid points per wavelength and on the right side, the error is a function of the number of layers. increasing the number of grid point beyond 500 does not decrease the relative error. Increasing the number of layers (right plot) does yield a lower relative error and the threshold is reached for all grid point settings for 3 layers per wavelength with an exception for the coarsest grid point resolution (375 points per wavelength) that shows atypical convergence behaviour.

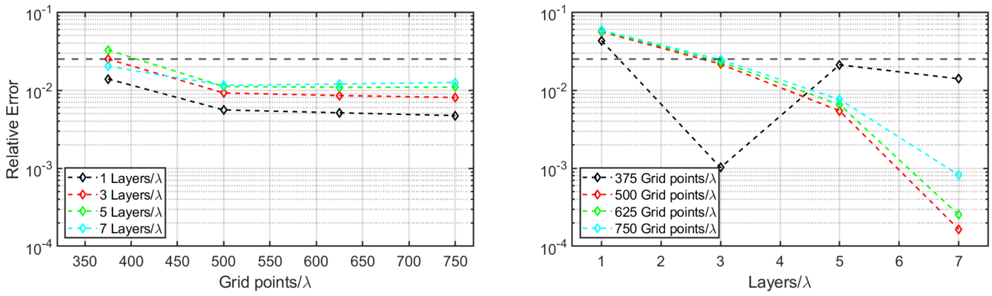

Figure A.1: Relative errors for the wave height H. The number of grid points (left) and amount of layers (right) per wavelength.

Regarding the phase angles, Figure A.2, similar results can be observed. However, more layers are required to reach the threshold. More grid points does not result in a lower error and is therefore unnecessary.

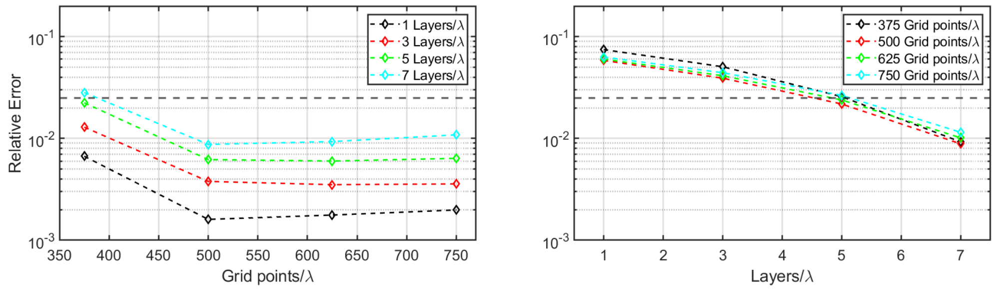

Figure A.2: Relative phase errors for the number of grid points (left) and amount of layers (right) per wavelength.

A.2. Irregular waves

Figure A.3 shows the significant wave height as a function of the amount of grid points (left) and the number of layers (right). Increasing the number of grid points generally decreases the relative error, which is not the case for the number of layers. However, the largest number of grid points layers per wavelength, results in the lowest error.

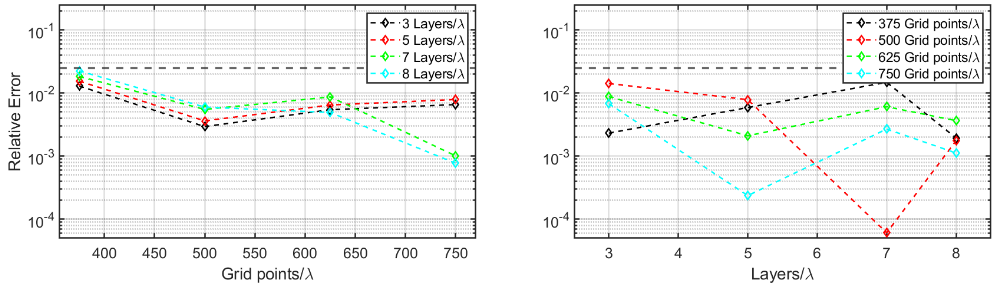

Figure A.3: Relative errors for the significant wave height H_{m0}. The number of grid points (left) and amount of layers (right) per wavelength.

The convergence behaviour of the peak phase angle for irregular waves, Figure A.4 is more typical. The results show that, similar to the significant wave height results, the finest grid resolution results in the lowest relative error overall.

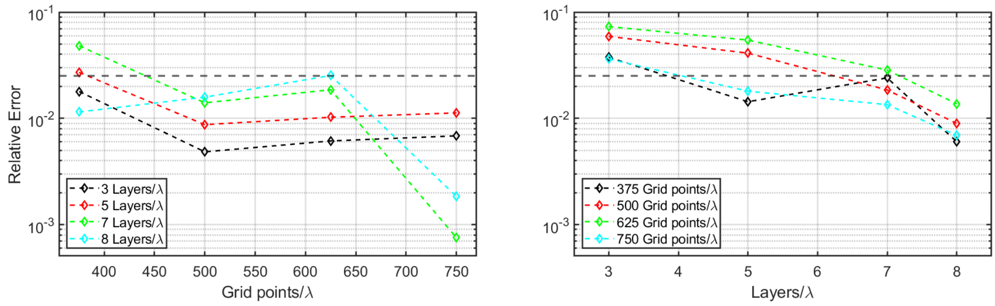

Figure A.4: Relative peak phase errors for the number of grid points (left) and amount of layers (right) per wavelength.